

University of Windsor

Scholarship at UWindor

Electronic Theses and Dissertations

Theses, Dissertations, and Major Papers

6-18-2021

A 2D CMUT Array for Liver Elastography

Sauparno Debnath
University of Windsor

Follow this and additional works at: <https://scholar.uwindsor.ca/etd>

Recommended Citation

Debnath, Sauparno, "A 2D CMUT Array for Liver Elastography" (2021). *Electronic Theses and Dissertations*. 8594.
<https://scholar.uwindsor.ca/etd/8594>

This online database contains the full-text of PhD dissertations and Masters' theses of University of Windsor students from 1954 forward. These documents are made available for personal study and research purposes only, in accordance with the Canadian Copyright Act and the Creative Commons license—CC BY-NC-ND (Attribution, Non-Commercial, No Derivative Works). Under this license, works must always be attributed to the copyright holder (original author), cannot be used for any commercial purposes, and may not be altered. Any other use would require the permission of the copyright holder. Students may inquire about withdrawing their dissertation and/or thesis from this database. For additional inquiries, please contact the repository administrator via email (scholarship@uwindsor.ca) or by telephone at 519-253-3000ext. 3208.

A 2D CMUT ARRAY FOR LIVER ELASTOGRAPHY

by

Sauparno Debnath

A Thesis

Submitted to the Faculty of Graduate Studies
through the Department of Electrical and Computer Engineering
in Partial Fulfilment of the Requirements for
the Degree of Master of Applied Science at the
University of Windsor

Windsor, Ontario, Canada

© 2021 Sauparno Debnath

A 2D CMUT Array for Liver Elastography

by
Sauparno Debnath

APPROVED BY:

S. Cheng
Department of Civil and Environmental Engineering

E. Abdel-Raheem
Department of Electrical and Computer Engineering

S. Chowdhury, Advisor
Department of Electrical and Computer Engineering

February 07, 2021

Declaration of Originality

I hereby certify that I am the sole author of this thesis and that no part of this thesis has been published or submitted for publication.

I certify that, to the best of my knowledge, my thesis does not infringe upon anyone's copyright nor violate any proprietary rights and that any ideas, techniques, quotations, or any other material from the work of other people included in my thesis, published or otherwise, are fully acknowledged in accordance with the standard referencing practices. Furthermore, to the extent that I have included copyrighted material that surpasses the bounds of fair dealing within the meaning of the Canada Copyright Act, I certify that I have obtained a written permission from the copyright owner(s) to include such material(s) in my thesis and have included copies of such copyright clearances to my appendix.

I declare that this is a true copy of my thesis, including any final revisions, as approved by my thesis committee and the Graduate Studies office, and that this thesis has not been submitted for a higher degree to any other University or Institution.

Abstract

Proper diagnosis of liver disease at an early stage is very crucial for its effective treatment. Chronic liver disease if not treated can often lead to cirrhosis. At present, liver biopsy is the main diagnostic procedure. A non-destructive, patient friendly diagnostic imaging technology is necessary. Piezo-electric transducer used for High Intensity Focused Ultrasound (HIFU) has a narrower bandwidth, thus a single transducer cannot be used for both imaging and HIFU operation. But capacitive micromachined ultrasonic transducers (CMUTs) can be used for both HIFU and imaging. In this thesis work, a unique design has been proposed where a first attempt has been made to design a 2D CMUT array for dual mode operation to detect liver cancer. First is the HIFU mode, where the device transmits a focused ultrasound to the target region in the liver just to momentarily deform (Strain) the liver tissue. Then the same device is switched to second mode which is an imaging mode. In this mode the ultrasonic image is captured using elastography process.

Analytical and 3D finite element analysis has been carried out in MATLAB and Intellisuite software, respectively. Bisbenzocyclobutene (BCB), a low K polymer is used as a primary structural material for the CMUT membrane and also for the structure of the CMUT. Gold is used as a top conductor placed on top of the diaphragm. Analytical calculations have been done on several CMUT cells in an array while designing the final array. Elements ranging from 8x8, 16x16, 32x32, and 64x64 have been analyzed. Finally, 64x64 array have been used for best results with a center frequency of 7.5 MHz which are in great agreement with FEA analysis done using Intellisuite software.

Dedication

To my parents and friends.

Acknowledgments

I would like to express my sincere appreciation to my supervisor Dr. Chowdhury, for his guidance and support. I am grateful to work in this research project under his supervision. His constant guidance and support throughout my research helped me to complete my work successfully.

I would like to thank my committee members Dr. Shaohong Cheng, Dr. Esam Abdel-Raheem for all their valuable comments and suggestions on my research. Their suggestion and comments helped me to present my work more efficiently. I want to extend my thanks to Andria for her administrative support throughout my research period.

I would also like to thank all my colleagues in MEMS Lab for their suggestion and help in every possible way during my research.

Contents

Declaration of Originality	iii
Abstract	iv
Dedication	v
Acknowledgments	vi
List of Tables	x
List of Figures	xi
Nomenclature	xiii
1 Introduction	1
1.1 Problem Statement	2
1.2 Motivation	3
1.3 Current Diagnostics Techniques for Liver Cirrhosis	4
1.3.1 Liver Biopsy	4
1.3.2 Blood Test	5
1.3.3 Imaging	5
1.4 Proposed solution	8
1.5 Research Objectives	9
1.6 Research Hypothesis	9
1.7 Principle Results	12
1.8 Thesis Organization	12
2 Ultrasound Elastography and Imaging	14
2.1 High Intensity Focused Ultrasound (HIFU)	14

2.1.1	Overview	14
2.1.2	HIFU Working Principles	15
2.2	Ultrasound Imaging	16
2.2.1	Overview	18
2.2.2	Medical use of Acoustic Imaging	18
2.2.3	Transient Elastography (TE)	21
2.3	General Concept of Phased Array	22
2.4	Ultrasound Imaging Modes	23
2.4.1	A-Mode	23
2.4.2	B-Mode	23
2.4.3	M-Mode	23
2.5	Ultrasonic Probes	24
2.5.1	Piezoelectric Transducer Probe	24
2.5.2	Capacitive Micromachined Ultrasonic Transducer(CMUT)	24
3	CMUT Phased Array Design	27
3.1	Specifications of Ultrasound imaging of soft tissue	27
3.2	Phased Array Design	28
3.2.1	Directivity analysis	29
3.2.2	Mechanical and Thermal Index	30
4	CMUT Cell Design	32
4.1	Cell design methodology	32
4.2	Center Displacement and Deflection profile	33
4.3	Capacitance	38
4.4	Resonant Frequency	39
4.5	Pull-in Voltage	41
5	CMUT Dual Mode Operation for diagnosis of Liver fibrosis	43
5.1	Liver Fibrosis	43
5.2	Transient Elastography	45
5.3	Dual Mode CMUT	45
5.3.1	Mode 1: HIFU	45
5.3.2	Mode 2: Imaging	50
5.4	Elasticity Estimation	55

5.5 Switching Circuit	60
5.6 Discussion	61
6 Conclusion	62
6.1 Summary	62
6.2 Future Works	63
Appendix	64
References	81
Vita Auctoris	87

List of Tables

1.1	Global mortality related to liver disease and liver cancer, 2015 [1].	2
2.2	Relative features between CMUT and Piezoelectric transducer	26
3.3	2D CMUT array specification	31
4.4	Material properties of CMUT cell	37
4.5	Design specification of CMUT cell	37
4.6	Comparison of capacitance	39
4.7	Comparison of natural frequency	39
5.8	FDA approved acoustic output exposure levels	46
5.9	Physical properties of different tissue. [2]	50
5.10	Elasticity estimation and fibrosis grade for chronic liver disease using a low frequency of 50Hz.	58
5.11	Phase delay of the Fourier transform of strain in the medium at 50Hz and 7.5MHz. .	59

List of Figures

1.1 Stages of liver disease [3]	3
1.2 CMUT Dual mode	9
1.3 Mode 1: HIFU	10
1.4 Mode 2: Imaging	11
2.5 HIFU schematic diagram [4]	15
2.6 Shear Wave Elastography [5]	19
2.7 Strain Elastography [5]	20
2.8 Transient Elastography set-up [6]	21
2.9 Piezoelectric transducer Crosssection	24
2.10 CMUT Cross-section	25
3.11 Phase array electronic (a) beam steering, and (b) focused beam [7]	28
3.12 Directivity of different array configuration	30
4.13 Cross section of a CMUT [8]	33
4.14 Cross section of a CMUT with deformed membrane [9]	33
4.15 Multilayer membrane	35
4.16 CMUT Cross Section [9].	36
4.17 Load deflection of the membrane	37
4.18 Load deflection of the membrane	38
4.19 Natural frequency FEA simulation	40
4.20 Mechanical Impedance	40
4.21 Electrical impedance	41
4.22 Coupling coefficient	42
5.23 Condition of liver at different stages of liver disease [10].	44

5.24 Pressure profile for a single CMUT cell	47
5.25 Pressure and Intensity profile for 8×8 CMUT array	48
5.26 Pressure and Intensity profile for 16×16 CMUT array	48
5.27 Pressure and Intensity profile for 32×32 CMUT array	49
5.28 Pressure and Intensity profile for 64×64 CMUT array	49
5.29 Receive voltage traces of point scatter for 64×64 CMUT array	51
5.30 Point spread function of the 2D array	52
5.31 Array imaging types [11]	52
5.32 Cyst B-mode image	54
5.33 Fetus B-mode image	55
5.34 Sector imaging with ultrasound probe [12].	56
5.35 Volumetric imaging with 2D array transducer [13]	56
5.36 Clinical significance of liver stiffness cut-offs in chronic liver diseases. When liver stiffness values range between 2.5 and 7 kPa, mild or absent fibrosis is likely, whereas when liver stiffness values are above 12.5 kPa, cirrhosis is likely. [14]	58
5.37 Comparative analysis of the phase delay of the Fourier transform of strain in the medium at 50Hz and 7.5MHz frequencies.	59
5.38 Schematics of HV switch [15].	60

Nomenclature

ϵ_m	Dielectric constant of the membrane
ϵ_t	Dielectric constant of the top electrode
λ	Wavelength
μ	Shear modulus
ω	Angular frequency
ρ	Density of the medium
σ	Poisson ratio
σ_0	Residual stress in the diaphragm
θ	Elevation angle
ε_0	Permittivity of free space
φ	Azimuth angle
A	Area of capacitor plates
a	Diaphragm half sidelength
c	Velocity of sound in the medium
c_m	Speed of ultrasound
D	Element pitch
d_m	Membrane thickness
d_t	Thickness of top electrode

D_{eff}	Effective flexural rigidity
d_{eff}	Effective gap
E	Young's modulus
f	Center frequency
F_{elec}	Electrostatic force
I	Acoustic Intensity
K	Kerf
k	Wave number
L	Element width (elevation)
P	Pressure amplitude
P_{ext}	External mechanical pressure
P_{peak}	Peak derated rarefaction pressure
t	Membrane thickness
u_0	Displacement amplitude
V	Bias voltage
ν	Poisson's ratio of the diaphragm material
V_s	Shear velocity
W	Element width (azimuth)
w_0	Diaphragm center deflection
Z	Characteristic acoustic impedance

Chapter 1

Introduction

This chapter contains the objectives of this thesis, the problem statement is explained and also the current solution to the problem is stated as well as their limitations. A proposed solution to the problem is presented in this chapter and finally, the thesis structure is presented.

The ultrasonic sensors market was valued at USD 1040.12 million in 2020 and is expected to reach a value of USD 2383.19 million by 2026, at a compound annual growth rate (CAGR) of 15.68%, during the forecast period (2020-2025). The global medical imaging market size was valued at USD 15.9 billion in 2020 and is expected to expand at a CAGR of 5.2% from 2021 to 2028. Major factors driving the industry are the increasing demand for early-stage diagnosis of chronic disease and rising aging demographics, which is expected to boost the demand for diagnostic imaging across the globe [16].

Ultrasonic transducers are present in everyday life in the form of level sensors, speed sensors, and medical imaging systems among others. Current ultrasonic transducers are usually built using piezoelectric materials and have proven to do a great job. CMUT technology can however broaden the applications and fields where ultrasounds could be used, in addition to avoiding undesired materials (Pb) and allowing easy integration with CMOS integrated circuits [17]. They offer many advantages in terms of bandwidth, fabrication of layer arrays, efficiency, and sensitivity. In recent years, thanks to advances in microfabrication techniques, the technology of CMUT has emerged as a competitive technology in the field of medical imaging [18].

In this thesis work, a 2D CMUT array with a center frequency of 7.5 MHz is designed which works in a dual mode of HIFU and elastography imaging. The diaphragm is made of low-K, B-staged polymer Bisbenzocyclobutene (BCB). The BCB is also used as a dielectric spacer and also as an insulating layer. The main objective of this research work is to integrate the HIFU and imaging

system in a single working CMUT transducer array. This will help in the reduction of cost for liver cancer diagnostics as previously it requires procurement of two separate devices, one for HIFU and the other for imaging, but this CMUT array can do the above two functions in one.

1.1 Problem Statement

Chronic liver diseases often result in fibrosis that may eventually lead to cirrhosis, a state that carries a risk of lethal complications, including hepatocellular carcinoma. These facts point out the clinical interest in quantifying hepatic fibrosis and detecting patients with cirrhosis. Cirrhosis can be defined as the end stage consequence of fibrosis of the hepatic parenchyma resulting in nodule formation and altered hepatic function [19]. Table 1.1 shows global mortality related to liver disease and liver cancer.

	Cirrhosis and the liver			HCC (Hepatocellular Carcinoma)
	Deaths(x1000)	% of total death	CDR - Crude Death Rate(per 100,000 population)	Deaths (x1000)
World	1162	2.1	15.8	788
East Asia & Pacific	328	2.0	14.4	547
Europe & Central Asia	115	1.2	12.7	78
Latin America & Caribbean	98	2.7	15.6	33
Middle East & North Africa	77	3.5	18.2	24
North America	50	1.7	14.0	27
South Asia	314	2.5	18.0	38
Sub-Saharan Africa	179	1.9	17.9	42

Table 1.1: Global mortality related to liver disease and liver cancer, 2015 [1].

The clinical manifestations of cirrhosis vary widely, from no symptoms at all, to liver failure, and are determined by both the nature and severity of the underlying liver disease as well as the extent of hepatic fibrosis. Up to 40% of patients with cirrhosis are asymptomatic and may remain so for more than a decade, but progressive deterioration is inevitable once complications develop including ascites, variceal hemorrhage or encephalopathy [19]. Figure 1.1 shows different stages of liver disease.

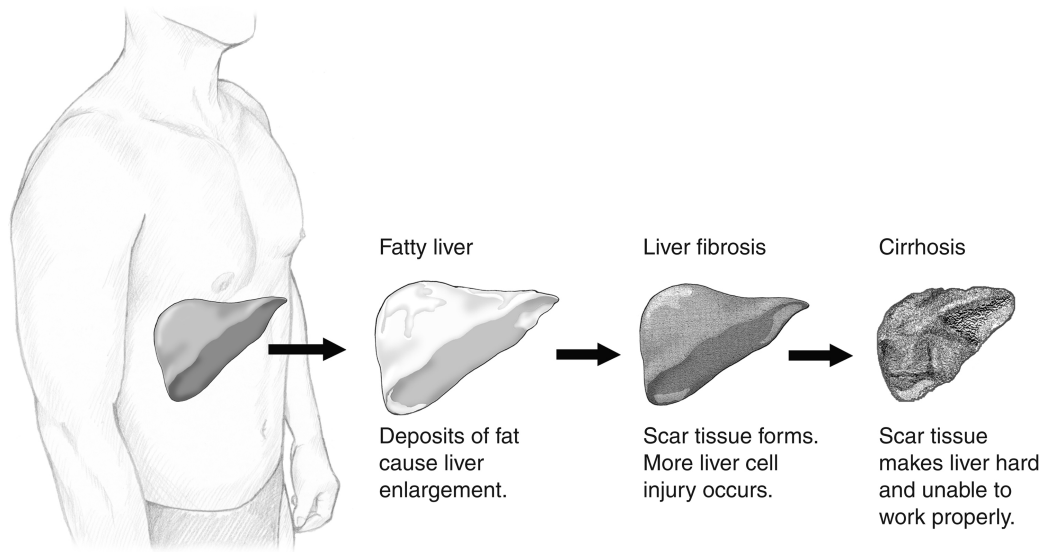


Figure 1.1: Stages of liver disease [3]

1.2 Motivation

The motivation behind this thesis work is to design a Capacitive Micromachined Ultrasonic Transducer (CMUT) array that helps in the correct diagnosis of liver cirrhosis in a non-invasive way and also at a lower cost. Cirrhosis in the liver is a great concern in the medical world as if it is not diagnosed early and correctly, it may lead to hepatocellular carcinoma, which is an early form of liver cancer which if untreated can ultimately lead to liver transplant or death. There are many forms of diagnosis of liver cirrhosis at present, these are liver biopsy, blood test, and also imaging. But all of these diagnosis methods cannot provide us with a correct result of the state of liver cirrhosis. A blood test is not an accurate way to diagnose liver disease as there is a lot of data collection error involved. At present biopsy is considered a "gold standard" in the diagnosis of liver disease. But biopsy itself is a painful process. Moreover, people who are already suffering from liver disease have to go through this painful biopsy process too which leaves patients in a traumatized condition. So a non-invasive but accurate process is needed for the diagnosis of liver cirrhosis. As it is a fact that ultrasound is a safe process in medical diagnostics, so using ultrasound for early detection of liver cirrhosis is possible. It does not use any harmful radiation for diagnosis and the acoustic intensity which is used in ultrasound is within the approved FDA limit. At present there are lots of ultrasonic transducers in the market which is being used but the most commonly used ultrasonic transducers are piezoelectric. But it's already proven from existing research that MEMS based transducers are superior to conventional piezoelectric transducers in several parameters such as fabrication cost,

frequency range, bandwidth, and thermal stability. Ultrasound elastography imaging captures the elasticity of the liver and assesses the state of liver disease. As at different stages of liver disease, the elasticity of the liver changes so an elasticity based method is very much effective for early detection of liver cirrhosis, which very crucial as it may prevent the onset of liver cancer. To resolve the above mentioned issues and implement the mentioned diagnostic process, this thesis aims to design a CMUT based ultrasound array for the diagnosis of liver cirrhosis based on the elastography technique.

1.3 Current Diagnostics Techniques for Liver Cirrhosis

Below are the methods that are currently being used for the diagnosis of liver Cirrhosis:

1.3.1 Liver Biopsy

Liver biopsy (LB) is the most common procedure performed in clinical hepatology. Histological assessment of the liver, and thus, LB is traditionally the “reference standard” in the diagnosis and management of parenchymal liver diseases. Definitive diagnosis often depends on LB, and much of understanding of the characteristic features and natural history of liver diseases is based on information obtained by serial liver biopsies. A variety of methods exist for getting a liver tissue specimen. These take account of a percutaneous method, a transvenous (transjugular or transfemoral) approach, and intra-abdominal biopsy (laparoscopic or laparotomic). All LB techniques require specific training to ensure appropriate-sized specimen retrieval and the lowest rate of complications [20].

Performance of LB requires an adequate sized and dedicated space suitable for focused physician effort as well as safe patient recovery. The most common approach for collecting a liver sample is percutaneous LB. A variety of needles are available for percutaneous LB; they are broadly classified into suction needles (Menghini, Klatskin, Jamshidi), cutting needles (Vim-Silverman, Tru-cut), and spring-loaded cutting needles that have a triggering mechanism. The choice of a specific type of needle depends in part on local preference. Cutting needles usually produce a larger sample and are less likely to yield inadequate specimens than are suction needles, but they probably result in more complications, probably because the needle remains in the liver longer [20].

Many complications arise after a biopsy procedure is done. The most common complication after percutaneous LB is pain. The mechanism of pain following percutaneous biopsy is most likely a

result of bleeding or possibly bile extravasation from the liver puncture wound, with subsequent capsular swelling. Transient hypotension, due to vasovagal reaction, can occur, particularly in patients who are frightened or emotional. Major complications were defined as life threatening or those that required hospitalization, prolonged hospitalization, or those that resulted in persistent or significant disability. Most serious complications occur within 24 hours of the procedure, and 60% happen within 2 hours; between 1% and 3% of patients require hospitalization [20].

1.3.2 Blood Test

While diagnosing liver cirrhosis, doctors sometimes recommend several blood tests. Blood tests that are done for diagnosis of liver cirrhosis can show abnormal liver enzyme levels, which may be a sign of liver damage. Doctors may suspect cirrhosis if there are increased levels of the liver enzymes alanine transaminase (ALT), aspartate transaminase (AST), and alkaline phosphatase (ALP), increased levels of bilirubin, or decreased levels of blood proteins. Doctors may perform a complete blood count, which can show signs of infection and anemia that may be caused by internal bleeding. Tests are also done for viral infections to see if the patient has hepatitis B or hepatitis C. And finally, blood tests for autoimmune liver conditions, which include the antinuclear antibody (ANA), anti-smooth muscle antibody (SMA), and anti-mitochondrial antibody (AMA) tests [21]. There are some additional tests done to diagnose cirrhosis. These are alpha-fetoprotein test, which is a specific blood protein made by fetal tissue and by tumors. This test may be done to predict the risk for primary liver cancer (hepatocellular carcinoma). It is also done to monitor the effectiveness of therapy in certain cancers, such as hepatomas (a type of liver cancer). Mitochondrial antibodies test indicates primary biliary cirrhosis, chronic active hepatitis, and certain other autoimmune disorders. Lastly, the Serum alpha-1 antitrypsin test (A1AT) test measures the levels of alpha-1 antitrypsin in the blood. This test is performed to help identify a rare form of emphysema in adults and a rare form of liver disease (cirrhosis) in children and adults [22].

1.3.3 Imaging

The classical role of many imaging modalities in liver cirrhosis diagnosis is the detection of morphological changes in the liver. The cirrhotic liver shows nodular hepatic contour, changes in volume distribution, including an enlarged caudate lobe and left lobe lateral segment, atrophy of the right and left lobe medial segments, widening of the fissures and the porta hepatis, and regenerative nodules. Secondary findings related to portal hypertension may present, including varices,

ascites, splenomegaly, fatty infiltration in the omentum and mesentery, edematous wall thickening of gastrointestinal tracts due to venous congestion, and intrahepatic arteriportal or arteriovenous shunts [23]. Basic imaging for the diagnosis of liver cirrhosis has developed over the last few decades, enabling early detection of morphological changes of the liver by ultrasonography (US), computed tomography, and magnetic resonance imaging (MRI) [23]. Diagnostic imaging can be classified into the following categories:

- **Magnetic Resonance Imaging (MRI)** has several advantages over other imaging techniques, including high-resolution images with excellent contrast against other soft tissue lesions and several different techniques facilitating the diagnostic evaluation of organ morphology, physiology, and function. As it is dependent on the detection of alterations in hepatic morphology, conventional MRI is limited to the diagnosis of earlier stages of liver fibrosis and is not suitable for disease staging. Calculation of the apparent diffusion coefficient (ADC) with diffusion-weighted imaging (DWI) using MRI can facilitate the assessment of liver fibrosis. One recent study showed that ADC values decrease with increasing stage of liver fibrosis from F0 to F4. However, no significant differences in ADC values were detected between the early stages of fibrosis [23].
- **Computed Tomography (CT)** is the most sensitive diagnostic tool for evaluating hepatic morphological changes. CT readily shows alterations in hepatic morphology and extra-hepatic manifestations related to portal hypertension. With liver cirrhosis progression, the nodularity of the liver surface and generalized heterogeneity of the hepatic parenchyma is visible. Changes in size and volume distribution are easily visible in a CT scan. In the early stages, the liver may appear normal. The limited spatial resolution of CT and MRI allow detection of only a relatively thick fibrous septum. Thick fibrous septa and confluent hepatic fibrosis showed low attenuation in non-enhanced CT. The boundary between fibrosis and normal parenchyma was more ambiguous in a contrast-enhanced scan. Therefore, it is difficult to perform texture analysis using CT. Perfusion imaging in liver fibrosis is based on the occurrence of substantial microcirculatory changes in this disease. These changes are caused by capillarization of the sinusoids, collagen deposits in the extracellular space of Disse, and contraction of activated stellate cells. Quantification of hepatic perfusion by dynamic CT has allowed separate evaluations of arterial and portal perfusion of the liver. Perfusion CT can be used to detect microcirculatory changes that occur in cirrhosis and help to differentiate low-grade fibrosis. Perfusion CT had several limitations. It suffered from the classic CT limitations: radiation, the use of iodinated contrast agents and limited scan coverage range [23].

- **Ultrasound sonography** is safe and relatively inexpensive imaging allowing annual or biannual tests in chronic hepatitis patients. Fibrosis of the hepatic parenchyma attenuates beam penetration, increases parenchymal echogenicity, and decreases vascular conspicuity. Liver cirrhosis is characterized by changes in liver volume distribution, surface nodularity, accentuation of the fissure, heterogeneity, bright and coarsening of the hepatic architecture, cirrhotic nodules including regenerative and dysplastic nodules, and signs of portal hypertension. The latest findings of liver cirrhosis were nodular surface, which was more sensitive on the under-surface of the liver than the superior surface [23]. Also, low and high frequency ultrasound based 2D and 3D sonography that relies on the reflection of acoustic pulses from tissues with different acoustic properties remains one of the key investigative tools for anatomical and functional diagnostic imaging of soft tissues.
- **Ultrasound Elastography** is now widely recognized as a reliable method to assess liver fibrosis. The principle of elastography is the shearing of the examined tissue, which induces a smaller strain in hard tissues than in soft ones. There are several commercial types of US elastography currently in use: transient elastography (TE), acoustic radiation force impulse imaging (ARFI), and shear wave elastography (SWE).

Transient elastography (TE) estimates liver stiffness by measuring the velocity of elastic shear waves in the liver parenchyma generated by the mechanical push. The propagation velocity is directly related to the stiffness of the medium, defined by the Young modulus. Stiff tissues exhibit higher shear wave velocities than soft tissues [24]. It is being used commercially by Echosens, Paris, France in their patented technology FibroScan®.

Acoustic Radiation Force Impulse (ARFI) imaging is a new method for quantifying mechanical properties of tissue, without manual compression, by measuring the shear wave velocity induced by acoustic radiation and propagating in the tissue. This technique has been developed by Siemens and is available on Acuson S2000 and S3000 ultrasound diagnostic imaging devices (Issaquah, WA, USA), and on the iU22 diagnostic imaging device developed by Philips (Bothell, WA, USA) [24].

Shear wave elastography (SWE) relies on shear wave propagation speed measurements in soft tissue. It was introduced in 2005 on the diagnostic Imaging device, called Aixplorer™ (SuperSonic Imagine, Aix-en-Provence, France). Unlike ARFI, SWE is based on the generation of a radiation force in the tissue to create the shear wave. [24].

At present, liver biopsy is the “gold standard” method to assess the grade of liver fibrosis. However, the use of liver biopsy has several limitations: physical and mental discomfort of the patients that

may lead to a high percentage of refusal, non negligible morbidity, and occasional mortality [19]. Also, there is the possibility of sampling error, which although possible, typically is not greater than one fibrosis stage in diffuse liver diseases. Sampling error is also possible when small biopsy samples are analyzed which may contain only one or two portal triads, or in which a nodule of hepatocytes is recovered but not the surrounding matrix. There is also inter-observer variability amongst hepatopathologists of up to $\sim 20\%$ in categorizing the degree of fibrosis. Moreover, a liver biopsy only provides static data, not dynamic findings reflecting the ongoing balance between matrix production and degradation, and does not sufficiently reveal underlying pathogenetic mechanisms [25].

There is a need for non-invasive, less expensive method of early detection of liver cirrhosis. Among other potentially interesting approaches, ultrasound based elastography seems to be one of the most promising. It is well known that liver stiffness is related to the degree of hepatic fibrosis, and palpation has been used for decades to establish a clinical diagnosis of hepatic fibrosis and cirrhosis [19].

1.4 Proposed solution

Transient elastography is different from other forms of ultrasound based elastography techniques. It uses mechanical force (transient vibration) to momentarily disturb the tissue. The use of a transient vibration presents several advantages. First, the transmitted elastic wave can be temporally separated from reflected elastic waves. Thus, the technique is less sensitive to boundary conditions than other elastographic techniques. Second, the acquisition time is short (typically less than 100 ms), which enables measurements to be made on moving organs [19].

Presently to perform the above procedure two separate systems are involved. First, a device that momentarily disturbs the tissue at the focus by the use of a focused ultrasound beam. Second, an ultrasound based imaging device generates an image based on the elasticity of the tissue. But using two separate systems become costly in the field of diagnostic medicine and become a burden for the patient. So in this thesis work an integrated 2D CMUT array has been proposed which works in dual mode for transient elastography. Figure 1.2 shows the conceptual diagram of the proposed dual mode operation of the CMUT.

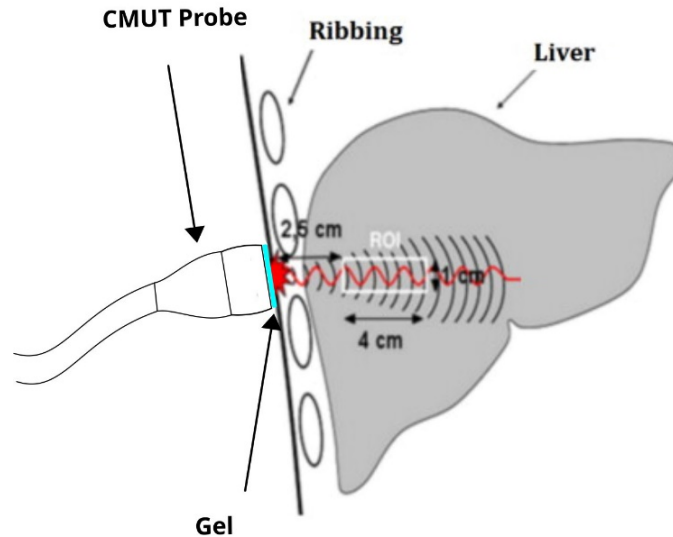


Figure 1.2: CMUT Dual mode

1.5 Research Objectives

- Design a dual mode 2D CMUT array that can be used in conjunction with appropriate micro-electronic signal processing algorithm to diagnose liver cirrhosis using ultrasound elastography.
- Use optimized acoustic pressure for the use of HIFU and accurately capture tissue elasticity in imaging mode.
- Improve accuracy of diagnosis of liver cirrhosis.
- Reduce cost for diagnosis of liver cirrhosis.

1.6 Research Hypothesis

As mentioned in the previous section, transient elastography, among other methods, is more suitable for early diagnosis of liver cirrhosis, so looking into this following research hypothesis has been developed:

- A CMUT array working in dual mode as HIFU and Imaging can be designed. Mode 1 is HIFU,

which is for inducing transient vibration towards the target tissue and momentarily disturb it, and mode 2 is for imaging system.

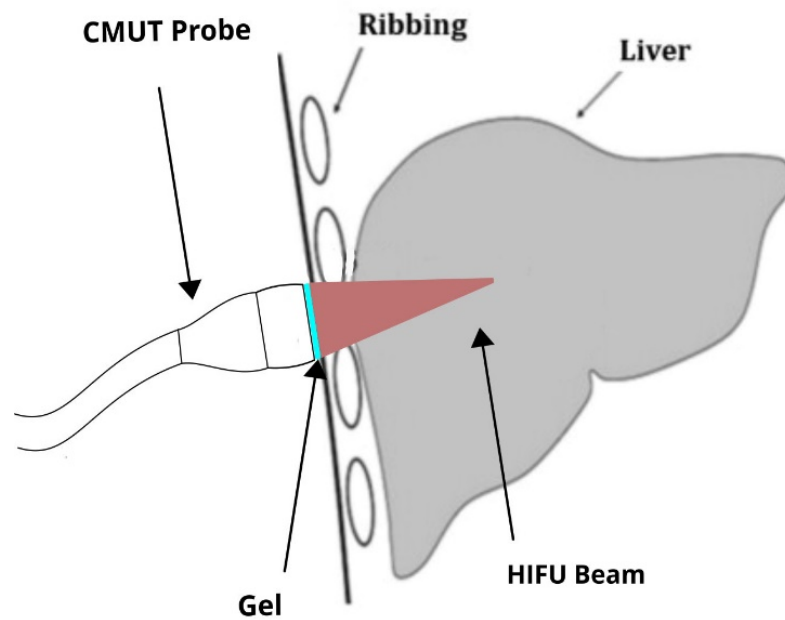


Figure 1.3: Mode 1: HIFU

- These dual mode 2D CMUT array can generate elastic image of the target tissue for elasticity measurement.

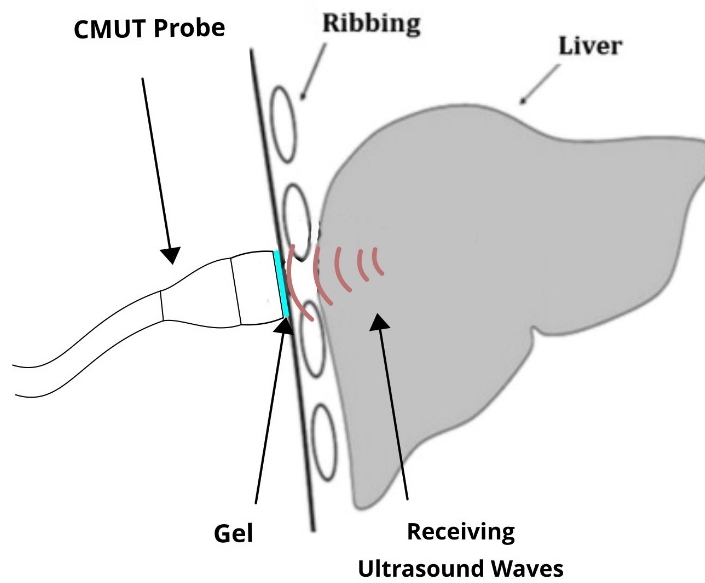
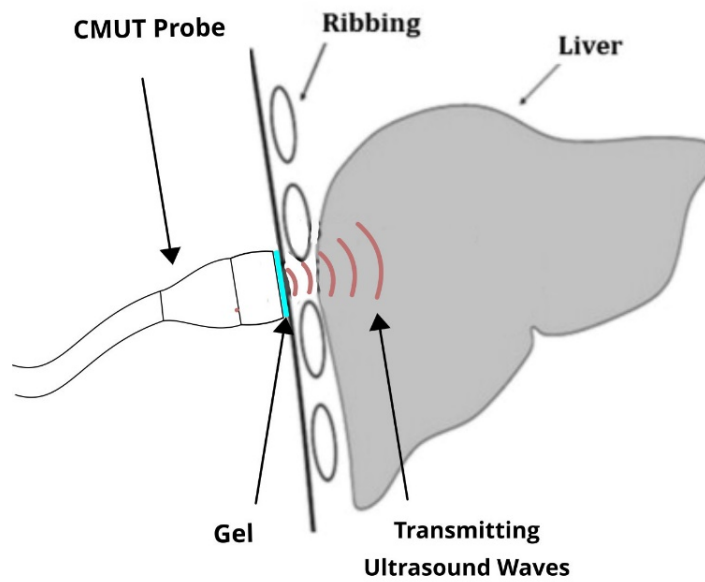


Figure 1.4: Mode 2: Imaging

- These dual mode setup can help us better diagnosis of liver cirrhosis at an early stage at a higher accuracy.

1.7 Principle Results

The results obtained from this research work are:

- A 64×64 array configuration has been selected for the CMUT design for dual mode operation having collapse voltage of 205.5 V, working at an acoustic intensity of 25 mW/cm^2 , and acoustic pressure of 0.845 MPa at focus at a distance of 25mm from the transducer surface.
- CMUT design has been simulated and verified to reach target specification.
- FEA of the CMUT cell has been performed to verify the analytical results.
- Acoustic intensity has been studied and considering the FDA limits, it has been correctly optimized to use with the designed array configuration and it is observed in simulation that correct acoustic pressure has reached target tissue.
- The designed CMUT array has been checked in imaging mode by using it on virtual phantom tissues and the target B-mode image has been successfully captured.

1.8 Thesis Organization

The thesis has been organized as follows:

Chapter 2 begins with an introduction of HIFU that has been used in this thesis work, its overview, and its working principle, a brief history of ultrasound imaging, its overview in the medical field, use of acoustic imaging in the field of medicine, different types of acoustic imaging and their limitations, ultrasound elastography, different types of elastography techniques, introduction to transient elastography. This chapter also provides a general concept of phased array and a brief idea of different ultrasound imaging modes. Lastly, this chapter concludes with CMUT working principle and comparative analysis with a piezoelectric transducer.

Chapter 3 contains phased array design, array directivity, mechanical and thermal index.

Chapter 4 CMUT cell design has been shown with FEA and analytical simulation in terms of center displacement, and displacement profile of the membrane, the capacitance between the electrodes of the CMUT cell, resonant frequency, and finally pull-in voltage calculation of the CMUT.

Chapter 5 contains the analytical calculations of the intensity of the CMUT cell while working in HIFU mode. It also contains MATLAB simulations of image acquisition of the target phantom tissue.

Chapter 6 provides a conclusion for the thesis and also provides an overview of its future prospects.

Chapter 2

Ultrasound Elastography and Imaging

This chapter highlights the concept of HIFU and its working principle. It also covers various forms of medical ultrasound imaging, various imaging modes, and finally an overview of different ultrasonic probes.

2.1 High Intensity Focused Ultrasound (HIFU)

The field of medicine is evolving toward greater use of noninvasive and minimal invasive therapies such as HIFU. Unlike radiofrequency or cryoablation, which is also used to ablate tissues, ultrasound is completely noninvasive and can be used to reach areas deep within the body, provided there is an acoustic window to allow the transmission of ultrasound energy [26].

As early as 1954, Lindstrom [27] and Fry [28] investigated the possibility of using high-intensity ultrasound for treating neurologic disorders in humans. Fry and colleagues are credited with the first application of HIFU in humans by producing elevated acoustic intensities in vivo by focusing ultrasound energy in a manner analogous to the way a magnifying glass can be used to focus light [26].

2.1.1 Overview

In comparing the differences in intensities of HIFU and diagnostic ultrasound, HIFU has significantly higher time-averaged intensities in the focal region of the ultrasound transducer. Typical diagnostic

ultrasound transducers deliver ultrasound with time-averaged intensities of approximately $0.1\text{--}100\text{ mW/cm}^2$ or compression and rarefaction pressures of $0.001\text{--}0.003\text{ MPa}$, depending on the mode of imaging (B-mode, pulsed Doppler sonography, or continuous wave Doppler sonography). In contrast, HIFU transducers deliver ultrasound with intensities in the range of $100\text{--}10,000\text{ W/cm}^2$ to the focal region, with peak compression pressures of up to 30 MPa and peak rarefaction pressures up to 10 MPa [26]. Figure 2.5 shows general schematics of a HIFU process.

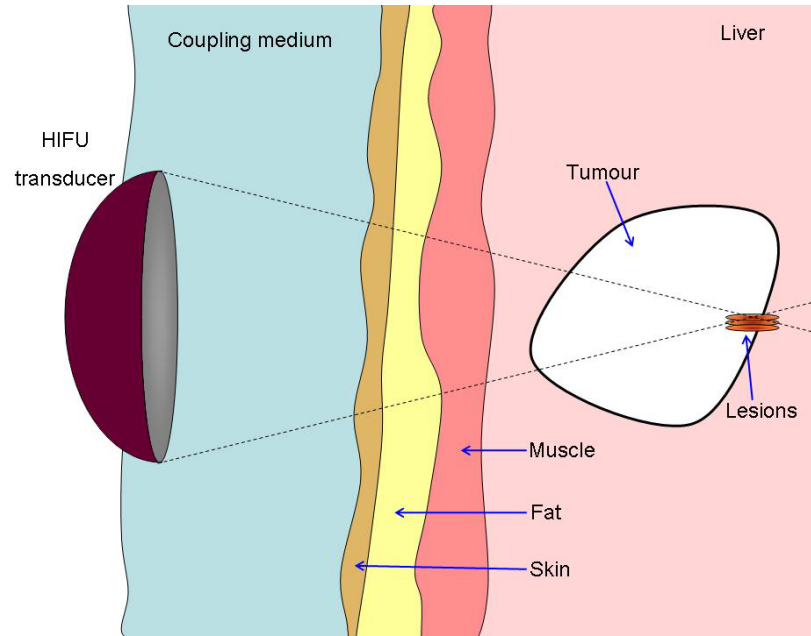


Figure 2.5: HIFU schematic diagram [4]

2.1.2 HIFU Working Principles

There are two main working mechanisms where HIFU is being used. Firstly, the thermal application, where the HIFU beam, when directed towards the target tissue, passes through the different layers of skin and tissues and reaches the target without causing any significant harm to any other surrounding organs. The target area of the focused beam develops lesion coagulative necrosis. This happens because of a rapid increase in tissue temperature due to the absorption of acoustic energy. An increase in tissue temperature for more than 60°C for 1 s results in irreversible cell death, which is the primary mechanism for tumor cell destruction in HIFU therapy. Thermal doses of $120\text{--}240\text{ min}$ at 43°C irreversibly damage and coagulate critical cellular protein, tissue structural components and the vasculature leading to immediate tissue destruction, however, the threshold varies with tissue type [29]. Another mode of application of HIFU is by using its mechanical effects.

Mechanical effects are associated with acoustic pulses at high intensities. There are different application areas where these high intensity pulses are used. First is the cavitation, where high intensity ultrasound pulses are directed towards a tissue which causes the formation of gas bubbles in an acoustic field in a low pressure region which causes damage to the surrounding tissue. Treatments such as shock wave lithotripsy (SWL) and histotripsy directly rely on cavitation. [30] Cavitation can generate very high pressures and temperatures, high shear stress, and create microstreaming jets of liquid that can cause pitting of the cell wall [31]. Also with the mechanical application of HIFU, when high intensity acoustic wave is focused towards a particular tissue, then the tissue experiences a momentary mechanical disturbance due to shear wave and then the image of the tissue is captured using an ultrasonic imaging method and from that, the elasticity of the target tissue is measured. This method is also known as ultrasound elastography.

Ultrasound waves while propagating through different layers of tissue in the human body, it interact uniquely with different layers depending on the extent to which those tissues resist the change in their mechanical impedance [8]. This characteristic of individual material is also known as characteristic acoustic impedance, Z (MRayl) and it can be defined as the product of the medium density, ρ and the velocity of sound, c in the medium

$$Z = \rho \times c \quad (2.1)$$

Within the tissue, while the ultrasound wave propagates, there are regions where the acoustic impedance changes, and these regions are known as acoustic boundaries. The ultrasound wave which propagates in the tissue can also be measured by its intensity, I (mW/cm²). The intensity of the ultrasound wave is the average power of the propagating wave per unit crosssection area over the surface perpendicular to the direction of propagating wave. Intensity is given by

$$I = \frac{P^2}{2\rho c} \quad (2.2)$$

where, P = Pressure amplitude of the ultrasound wave; and ρ = density of the medium.

2.2 Ultrasound Imaging

In the late 1940s, after World War II, a few scattered enthusiasts recognized the potential of ultrasonic energy to provide information that could be useful in medical diagnosis. The efforts of these innovators resulted in new concepts and in unique early images that motivated both the manufacturers of instruments and the clinical pioneers to begin to establish meaningful clinical applications

for this new phenomenon. The early successes of these individuals created a momentum that encouraged additional users and provided a firm foothold and broadened horizons for this emerging technology [32]. Although discovered 12 years before the X-ray (1883.), the ultrasound is a much later found application in medicine. The first practical application of ultrasound is recorded during World War I in detecting submarines [33]. In 1912, Lewis Richardson patented an ultrasonic underwater detection device [34]. In 1914, Reginald Fessenden detected an iceberg from 3 km away by echo-ranging with a moving-coil transducer. In 1918, Constantin Chilowsky and Paul Langevin detected a submarine at 1.5 km using a piezoelectric transducer. During the 1930s many ocean-going liners are fitted with echo-ranging devices [8]. During the 1940s sonar is widely used for submarine detection in World War II [34]. The earliest pioneers in the United States included three physicians, John Wild, a surgeon, George Ludwig, an internist, and Douglas Howry, a radiologist [32]. Of this group, Douglas Howry had the greatest influence on the other pioneers in radiology. In the late 1940s, he left a formal residency program at Denver Veterans Administration Hospital to devote more time to ultrasound research. Working in his basement with engineers William Rodemick Bliss and George Posakony, Howry pursued his goal of using ultrasound to produce accurate anatomic pictures of soft-tissue structures [32].

The successful application of ultrasonic pulse techniques and the echo-ranging principle to underwater detection and ranging and to the localization of flaws in metals prompted an investigation of the use of an analogous technique for diagnostic purposes in medicine and surgery [35]. In 1951, engineers developed a two-dimensional compound ultrasound scanner. It was incorporated with an immersion tank by using a cattle-watering container with an ultrasonic transducer mounted on a wooden rail. The transducer, immersed in the tank with the object under study, moved horizontally along the rail [32]. This method allowed the use of a large transducer (better sensitivity) that could be held away from the patient. The greater distance between the transducer and the patient allowed for better focusing of the ultrasound beam [32]. In 1942, one of the pioneers of ultrasound, Karl Dussik attempted ultrasonic transcranial brain imaging using 1.2 MHz pulses of 100 ms duration [8]. George Ludwig published a report on the use of ultrasound for diagnosis, which includes a mean value of tissue sound speed of 1540 m/s and recommended an optimal frequency of 1 and 2.5 MHz [48]. In 1953, I. Edler and C. Hertz detected heart motions as the first example of echocardiology [36]. Followed by Sven Effert in Germany in 1956, Claude Joyner and John Reid at the University of Pennsylvania in 1957, and Chih-Chang Hsu in China, designing their own A- and later on M-mode equipment. Similarly, A-mode devices were used in ophthalmologic investigations by Henry Mundt Jr. and William Hughes at the University of Illinois in 1956, Arvo Oksala in Finland in 1957, and Gilbert Baum and Ivan Greenwood in 1955 [8]. These uses were all in the 1950s

and largely predated clinical applications in the abdomen and pelvis. In 1962, Shigeo Satomura suggested blood flow measurement using Doppler-ultrasound. In 1965, the first real-time scanner was built by Siemens. During the 1980s ultrasound screening for pregnant women was introduced. During the 1990s tissue harmonic imaging improves image resolution. During 2000s Real-time 3D ultrasound imaging [8].

2.2.1 Overview

Generally, the ultrasound frequency range varies from more than 20 kHz to several gigahertz. A human being can hear the sound range up to 20kHz. Medical use of ultrasound started long back. Initially, its use was limited but with the development of various technologies related to medical ultrasound, now it is being used in almost all fields of medicine. Higher frequencies have a correspondingly smaller wavelength and can be used to make sonograms with smaller details. Sonography is a form of ultrasound imaging technique that is used to effectively image soft tissues of the human body. Sonographers typically use a hand-held probe (called a transducer) that is placed directly on and moved over the patient. A water-based gel is used to couple the ultrasound between the transducer and patient [33].

2.2.2 Medical use of Acoustic Imaging

Ultrasound waves are a type of acoustic energy travel in a form of longitudinal wave propagation. The frequency range for its diagnostic and therapeutic application is between 1 to 60 MHz [8]. Two decades ago, in the field of medical imaging, the terms acoustic imaging and ultrasonic imaging were synonymous. In the 1990s, a new acoustic imaging technology started to emerge that was based on shear (or transverse) acoustic waves [37].

Conventional acoustic imaging uses ultrasound to generate real time images of internal organs. The sound waves propagate through our skin layers and it exploits the impedance mismatch at different tissue layers to generate 2D and 3D images. Types of acoustic imaging are:

- Ultrasonography
- Photoacoustic imaging (PAI)

There are limitations to conventional acoustic imaging:

- Poor image quality due to higher acoustic attenuation.
- Presence of gas bubbles results in bad image quality.

- Operator skills are highly important.
- Entropy production due to acoustic attenuation results in information loss of final image [38].

Thus to address the above limitations of conventional acoustic imaging, a better technique such as ultrasound elastography is emerging gradually.

2.2.2.1 Ultrasound Elastography

Elastography is the set of techniques by which tissue stiffness is estimated from the Young's modulus (E). Young's modulus can be expressed as:

$$E = 3\rho V_s^2 \quad (2.3)$$

where V_s = shear velocity; and ρ = mass density. Ultrasound elastography can be classified in two broad categories:

- Strain based
- Shear wave based

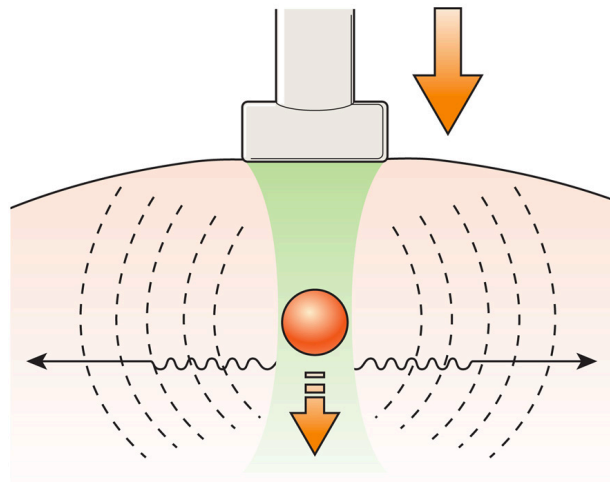


Figure 2.6: Shear Wave Elastography [5]

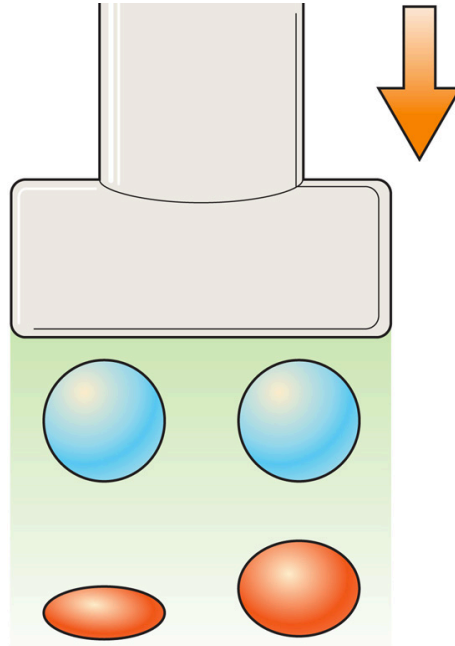


Figure 2.7: Strain Elastography [5]

2.2.2.2 Shear wave elastography (SWE)

Shear wave elastography uses Compressional Wave Speed which travels at high speed through soft tissue (1450 - 1550 m/s) to generate conventional B-mode image [39]. The propagation velocity of this wave depends upon tissue stiffness. Shear wave is monitored at different locations along the ultrasound probe, permitting the estimation of shear wave velocity. Figure 2.6 shows schematic diagram of a shear wave elastography.

2.2.2.3 Strain Elastography (SE)

In strain elastography (SE), external pressure is applied to measure the tissue stiffness. As the strain is applied to the soft tissue, it gets momentarily deformed. Thus, strain estimates are calculated as a function of depth at the center frequency. Strain ratio is also calculated which is the ratio between strain in a tissue region and strain in any other reference region. When the strain ratio is greater than 1, then it is the indicator of low strain and high stiffness. Figure 2.7 shows strain elastography.

Another form of elastography technique that uses the strain ratio is Transient Elastography (TE).

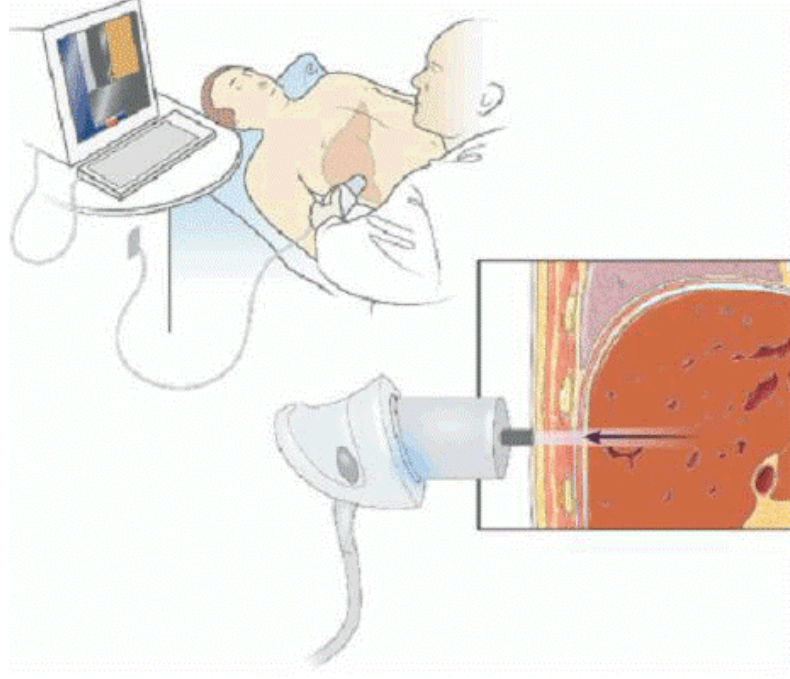


Figure 2.8: Transient Elastography set-up [6]

2.2.3 Transient Elastography (TE)

Transient elastography (TE) measures the stiffness of the tissue region to determine the extent of damage of the tissue. With this technique, parameters like anisotropy, viscosity or elastic non-linearity can also be obtained. Shear wave propagation velocity is used to measure the tissue stiffness and tissue stiffness increases with the increase in fibrosis of liver [39]. So, this elastography technique is very much useful to detect Hepatocellular carcinoma, which is an early form of liver cancer.

Acoustic wave interacts differently with different tissues while propagating through various layers of the human body. While propagating through different mediums in the human body it generates pressure disturbances which in turn creates compression and expansions in the medium. These pressure disturbances can be seen as a wave motion on the medium. For simplicity, we assume a linear, elastic, isotropic, and homogeneous medium [37],

$$\rho \frac{\partial^2}{\partial t^2} u(\mathbf{x}, t) = (\lambda + \mu) \nabla (\nabla \cdot u(\mathbf{x}, t)) + \mu \nabla^2 u(\mathbf{x}, t) \quad (2.4)$$

where ρ = mass density; λ_L and μ_L = Lamé parameters; t = time; and \mathbf{x} = spatial vector defines as

$\mathbf{x} = [x, y, z]$. Also wave equation is given by [37]

$$u(\mathbf{x}, t) = u_0 e^{i(\omega t - k\mathbf{x})} \quad (2.5)$$

where u_0 = displacement amplitude; ω = angular frequency; and k = wavenumber.

2.3 General Concept of Phased Array

Ultrasonic transducer arrays have different geometrical configurations according to their focal length and are used in the appropriate field of application. When the object to be scanned is much bigger than the transducer itself, the transmitted ultrasonic wave beam is steered intentionally towards the target object for better resolution. There are two major ways to steer the beam. The first is mechanical beam steering and the other one is electronic beam steering. However, mechanical steering is slow and expensive. A more effective approach to conduct inspections and form images is to use an ultrasonic phased array, where the sound beam can be manipulated electronically [7].

In a phased array setup, the ultrasonic transducer is composed of an array of small elements, where each element can be separately driven and the response of each element independently received. If each of the elements is driven identically so that the driving electrical pulses travel in unison and all arrive at the piezoelectric elements at the same time (no relative delay between pulses) then each small element of the array acts effectively as a point source and radiates a spherical wave and these spherical waves combine to form a traveling wave pulse [7]. By varying the relative time delays, Δt_i , of the driving pulses (where the ensemble of delays is called a delay law), the ultrasonic phased array can electronically steer the sound beam generated in different directions, without requiring any movement of the transducer itself [7]. With this time delay applied, so that all of the signals occur at the same time, then they can be summed to generate a single, large output signal [8]. This delay law is then analogous to what would happen with a focused single element transducer on reception. Because an ultrasonic phased array can transmit/receive with each element of the array independently of the other elements, it also is possible to apply individual amplitude weights, \tilde{C}_i , to the elements on either sound generation and reception (or both). The ensemble of such amplitude weights is called an apodization law [7].

2.4 Ultrasound Imaging Modes

Displaying the captured image properly is very important for proper diagnostics. ultrasound used different modes to display its image. Some of them are given below:

2.4.1 A-Mode

A-mode or amplitude mode is one of the simplest among ultrasound. It is a display of amplitude spike of different heights. The amplitude of the spike represents the relative echo strength and the time scale provides a relative measure of the distance of the associated reflecting boundary from the transducer [40].

2.4.2 B-Mode

B-mode or brightness mode, signals from returning echoes are displayed as dots of varying intensities. The spike of the A-mode is replaced by a small dot. The intensity of a dot (the brightness) is a relative measure of echo size, with large echoes appearing as very bright dots, while at the other extreme non-reflectors appear dark. When the beam is swept across a selected section of the subject (the process of scanning), different dot lines are created for each scan line. The combined information from different scan lines provides a 2-D image of the cross-section through which the beam sweeps [40].

2.4.3 M-Mode

M-mode or motion mode is used to generate an electronic trace of a moving object lying along the path of the ultrasound beam. The transducer is placed in one fixed position to the moving structure. Returning echoes are displayed in the form of dots of varying intensity along a time base as in B-mode. Dots for stationary reflectors will remain in the same positions along the time base, but dots for reflectors that move in the direction of the scan line will change their positions along the time base because their distances from the transducer will be changing with time. The M-mode provides 1-D information along the beam path. For a moving structure to be detected, it must lie along the ultrasound beam path. The M-mode is particularly useful in examining cardiac motion [40].

2.5 Ultrasonic Probes

Below are the two types of ultrasonic transducer probes which are most commonly used in different applications.

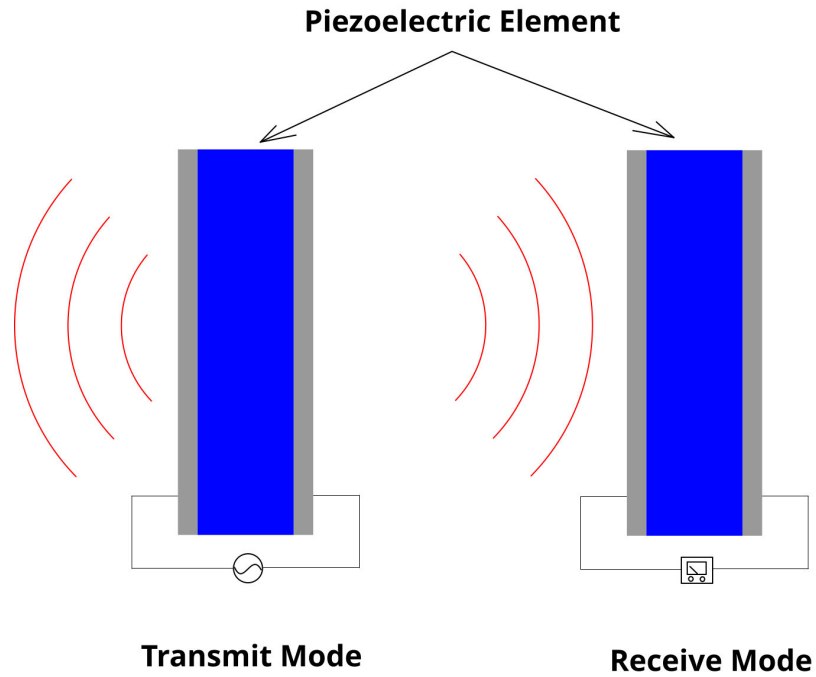


Figure 2.9: Piezoelectric transducer Crosssection

2.5.1 Piezoelectric Transducer Probe

A piezoelectric transducer is made of a single crystal where electric polarity is produced when pressure or voltage is applied. When a voltage is applied to piezoelectric materials (PZT or Lead Zirconate Titanate, Barium Titanate, Lithium Niobite) they accumulate charges, and the crystal shrinks and expands and thus create ultrasound and when an ultrasonic wave pressure is incident on the piezoelectric material, it causes strain on the material and generates piezoelectricity.

2.5.2 Capacitive Micromachined Ultrasonic Transducer(CMUT)

Capacitive micromachined ultrasonic transducers (CMUTs) have emerged as an alternative to conventional piezoelectric transducers. They offer many advantages in terms of bandwidth, fabrication of layer arrays, efficiency, and sensitivity. Piezoelectric crystals, ceramics, polymers, and piezo

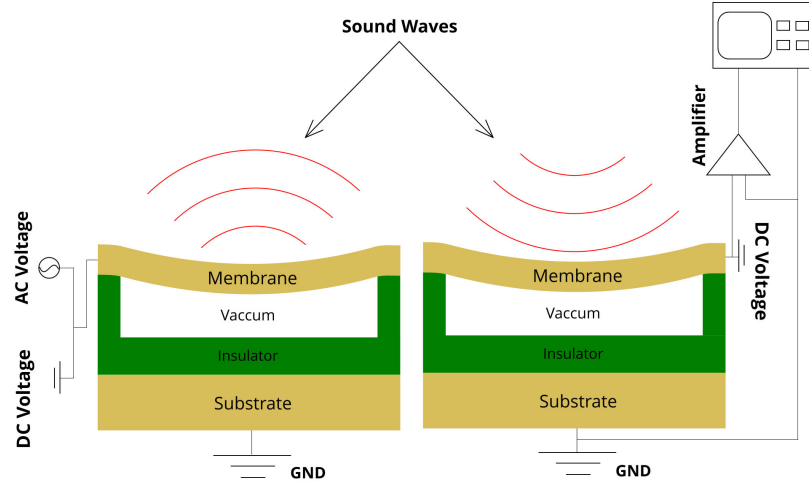


Figure 2.10: CMUT Cross-section

composite materials have long dominated ultrasonic transducer technology, especially in medical ultrasound imaging. Thanks to advances in microfabrication techniques, the technology of capacitive micromachined ultrasonic transducers (CMUTs) has emerged as a competitive technology in the field of medical imaging, NDT, HIFU, and many other applications [18]. It is a variable capacitor constructed with a vibrating diaphragm separated from a fixed backplate by a vacuum or an airgap. The diaphragm is electrically or acoustically vibrated to generate or receive an ultrasound at the desired frequency.

The electrostatic force generated on the plates of a capacitor is proportional to the square of the applied voltage, the area of the capacitor, and the permittivity of the material between the plates, and inversely proportional to the square of the separation between the plates [18]:

$$F_{elec} = \frac{\epsilon_0 A V^2}{2d^2} \quad (2.6)$$

where ϵ_0 = permittivity of free space; A = area of capacitor plates; V = applied bias voltage; and d = distance between the capacitor plates.

The above equation can also be represented in terms of alternating current (AC) and direct current (DC) voltage components. As working of CMUT requires both DC and AC bias voltage, so equation (2.6) can also be written as [18]:

$$F_{elec} = \frac{\epsilon_0 A}{2d^2} (V_{DC}^2 + 2V_{DC}V_{AC} + V_{AC}^2) \quad (2.7)$$

The first term in parenthesis represents the static force, the second term represents the excitation

force proportional to the applied AC voltage, and the last term represents the harmonic contribution of the AC voltage, which also contributes to the static force. When the DC bias voltage is much larger than the AC excitation, the harmonic contribution can be ignored [18].

	CMUT	Piezoelectric
Fabrication Technology	MEMS	Ceramic
Array Fabrication	Easy and low cost	Difficult and expensive
Fractional Bandwidth	High	Low
Bandwidth	Wide	Moderate
Uniformity	High	Moderate
Thermal Stability	High	Low
IC Integration	Yes	No
Output pressure	Improving	High

Table 2.2: Relative features between CMUT and Piezoelectric transducer

Chapter 3

CMUT Phased Array Design

3.1 Specifications of Ultrasound imaging of soft tissue

Noninvasive, ultrasound-based methods for visualizing and measuring tissue elasticity are becoming more and more common in routine practice. Using hepatic shear wave elastography, cut-off levels can help to detect the degree of relevant fibrosis ($F \geq 2$) with a diagnostic accuracy using the area under the reader operating characteristic (AUROC) of 87% and cirrhosis ($F=4$, AUROC 93%) [41]. Ultrasonic waves in the frequency range 1–20 MHz are widely used in clinical medicine for diagnostic, therapeutic, and destructive purposes, and therefore their propagation characteristics are of particular interest and have been most fully studied. From a knowledge of the wave velocities and of the degree to which tissues absorb, scatter, and reflect ultrasound, it is possible, in principle, to predict how ultrasound propagates within, and interacts with, the body [42]. When ultrasound waves propagate through tissue, it experiences some resistance, which is known as acoustic impedance. Every tissue has a different acoustic impedance. While designing an ultrasonic transducer array, the acoustic impedance factor should be taken into account. According to [42], the peak rarefaction pressure of the diagnostic ultrasound generated from a transducer array can be in the range of 0.5-5 MPa with maximum acoustic power in the range of 4-256 mW. Also according to [43] the amount of acoustic intensity, which is measured in I_{ISPTA} (derated Spatial-Peak Temporal-Average Intensity), sent into the patient is below the official level of $< 94mW/cm^2$.

3.2 Phased Array Design

In this thesis, the center frequency of 7.5 MHz has been chosen for optimal performance of this CMUT array for Liver elastography. While designing a transducer array, along with ultrasound emission parameters, the physical design parameters of the array must be taken into equal importance so that a proper final image of the target tissue is obtained. At the time of designing the array, the element pitch, the kerf length have been chosen in such a way that we avoid grating lobes and we get the optimal result.

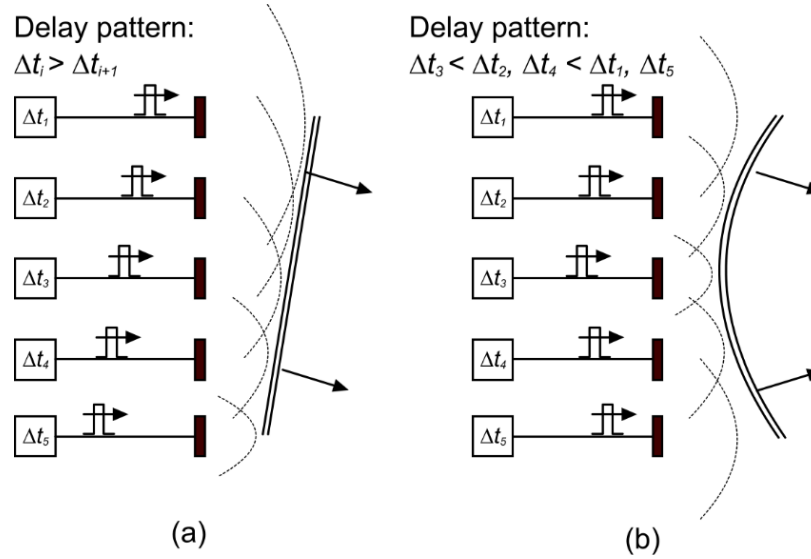


Figure 3.11: Phase array electronic (a) beam steering, and (b) focused beam [7]

A phased array of ultrasonic transducers for diagnostic imaging unlike single element transducers is capable of dynamic focusing and steering the beam electronically to achieve higher resolution image and minimum scan time. In a phased array setup, the ultrasonic transducer is composed of an array of small elements, where each element can be separately driven and the response of each element independently received. If each of the elements is driven identically so that the driving electrical pulses travel in unison and all arrive at the piezoelectric elements at the same time then each small element of the array acts effectively as a point source and radiates a spherical wave. These spherical waves combine to form a traveling wave pulse. However, by varying the relative time delays, Δt_i of the driving pulses the ultrasonic phased array can electronically steer the sound beam generated in different directions without requiring any motion of the transducer itself as shown in figure 3.11(a). With an appropriate non-linear delay law, the same array can also generate a focused sound beam as shown in figure 3.11(b). A more complex combination of these delay laws

can simultaneously perform both beam steering and focusing [8].

3.2.1 Directivity analysis

The directivity is a crucial parameter for CMUT design, and it describes that the amplitude of its transmitting response or receiving response is varying with an azimuth, which is also a kind of attribute in the far field. This is usually evaluated by using the directivity function, directivity diagram, beam width, side lobe level, and so on [44]. A single CMUT cell cannot meet requirements for transmitting sufficient power, so a CMUT array of N identical elements arranged at equal intervals is used. According to the Huygens principle, the directivity functions of a CMUT 2D array can be expressed by [45]:

$$D = \frac{4 \sin\left(\frac{kM_a}{2} \cos\theta \sin\varphi\right)}{k^2 M \sin\left(\frac{ka}{2} \cos\theta \sin\varphi\right)} \times \frac{\sin\left(\frac{kd_a}{2} \cos\theta \sin\varphi\right)}{d_a \cos\theta \sin\varphi} \times \frac{4 \sin\left(\frac{N_b}{2} \sin\theta \sin\varphi\right)}{N \sin\left(\frac{kb}{2} \sin\theta \sin\varphi\right)} \times \frac{\sin\left(\frac{kd_b}{2} \sin\theta \sin\varphi\right)}{d_b \sin\theta \sin\varphi} \quad (3.8)$$

where d_a and d_b are both adjacent elements spaced in the 2D array in the element side length direction, θ is the Elevation angle, φ is the Azimuth angle, $k = \frac{2\pi}{\lambda}$ is the spatial frequency, M is the number of elements in x-direction, and N is number of elements in y-direction. The directivity pattern of the array have been calculated using Transducer Array Calculation (TAC) GUI toolbox in MATLAB [46]. The directivity pattern of different array geometry has been shown in the figure 3.12. From the figure, it can be seen the effect of the number of array elements on the main lobe width and also on the side lobes. As the width of the main lobe reduces, the power of the array at focus increases.

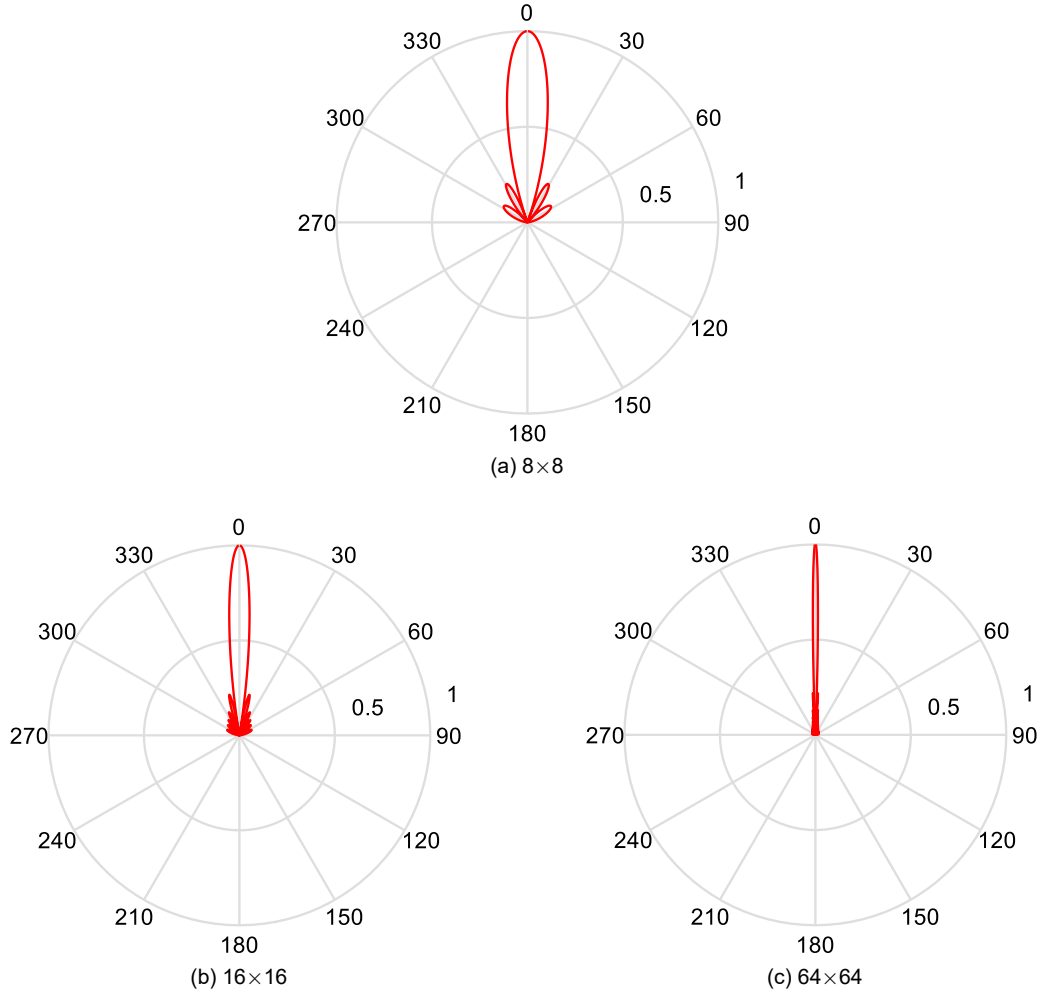


Figure 3.12: Directivity of different array configuration

3.2.2 Mechanical and Thermal Index

The soft tissue thermal index (TIS) and the mechanical index (MI), have been designed to inform the user of conditions which might give rise to safety concerns during any scanning session. It is very important to design and make safe equipment, and it is also very important that the users operate the equipment safely [42]. MI is intended to indicate the probability of occurrence of inertial cavitation, while TIS is an indicator of the likely maximum temperature rise in tissues exposed to the ultrasound field. Although these indices can provide useful information to the user, they are not perfect and are based on a set of very specific assumptions [42]. MI [8] and TIS [47] can be calculated by using the equations:

$$MI = \frac{P_{peak}}{\sqrt{f(MHz)}} \quad (3.9)$$

$$TIS = \frac{W_0 f}{130} \quad (3.10)$$

where P_{peak} is the derated peak rarefaction pressure (in MPa); f is the acoustic working frequency; W_0 is the maximum value of time average output power emitted from any 1 cm length of the radiating aperture in the scan direction.

After calculating all the above parameters, below are the values of the target CMUT array design:

Symbol	Parameters	Value
f	Center frequency	7.5 MHz
c	Acoustic speed in medium	1500 m/s
λ	Wavelength	200 μm
N	Number of elements	4096
A	Aperture	5.064 mm
D	Element pitch	80 μm
W	Element width (azimuth)	24 μm
L	Element width (elevation)	24 μm
K	Kerf	56 μm
TI	Thermal index	0.23
MI	Mechanical Index	0.22

Table 3.3: 2D CMUT array specification

Chapter 4

CMUT Cell Design

4.1 Cell design methodology

CMUT is a dynamic capacitor where the membrane vibrates when a bias voltage or an ultrasonic pressure is applied on it, and thus the capacitance between the membrane and its backplate changes. This capacitance calculation is essential for the correct calculation of CMUT's transmit and receive sensitivity.

To determine the capacitance change, it is first necessary to calculate the center displacement of the membrane. The diaphragm's center displacement is then used to calculate the deflection profile of the square diaphragm. The capacitance is then obtained by integrating an infinitesimal area of the deformed membrane where the parallel plate approximation holds. The load-deflection model of a rigidly clamped square diaphragm is used initially to design the approximate behavior of the CMUT considering geometry and materials. The developed geometry is then modeled using 3-D electromechanical FEA and is later used to study the behavior of the membrane in the presence of its neighbors in the design space [9].

The main parameter is the center frequency. All the analyses were carried on keeping in mind the required center frequency of 7.5MHz. The side length, air gap, and thickness of the diaphragm are important factors in designing a CMUT cell for a given center frequency. The design specification shown in Table 4.5 is chosen specifically after a lot of analysis so that the CMUT cell works in the required frequency.

Figure 4.13 shows the cross-section geometry of a CMUT cell. Here a low-K insulator BCB has been used as a structural material for the diaphragm as well as a dielectric spacer between the top and bottom electrode of the CMUT. Material physical properties have been shown in the Table 4.4.

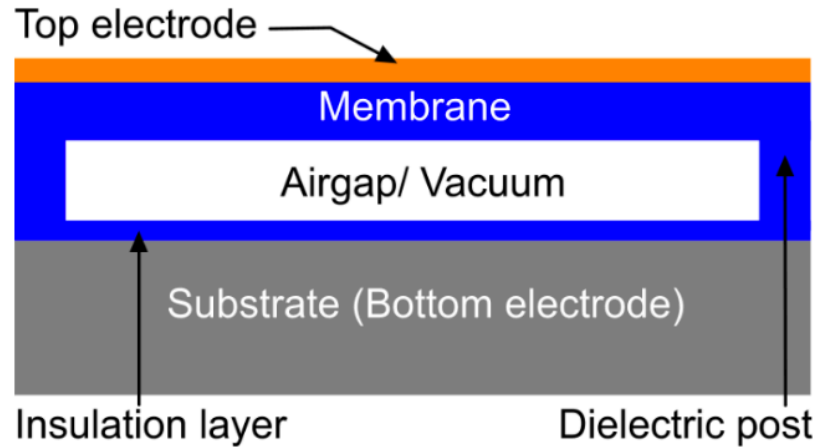


Figure 4.13: Cross section of a CMUT [8]

4.2 Center Displacement and Deflection profile

The diaphragm is assumed to be homogeneous and isotropic with perfect edge conditions. It is assumed that the clamped edges hold the diaphragm rigidly against any out-of-plane rotation or displacement at the edges but allow displacement parallel to the diaphragm plane. At the edges, out-of-plane displacement is zero and the tangent plane to the displacement surface along the edge coincides with the initial position of the middle plane of the diaphragm.

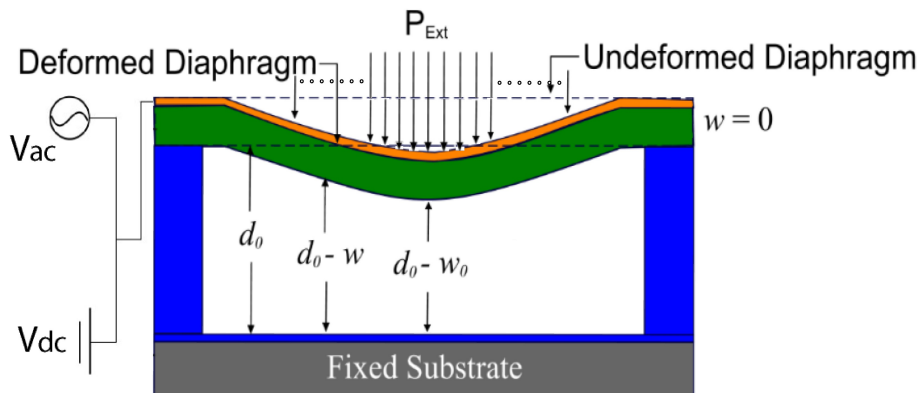


Figure 4.14: Cross section of a CMUT with deformed membrane [9]

Boundary conditions imposed by the clamped edges can be expressed mathematically as [48]:

$$\begin{aligned}
w(x = \pm a, \forall y) &= 0 \\
w(y = \pm a, \forall x) &= 0 \\
\frac{dw}{dx}(x = \pm a, \forall y) &= 0 \\
\frac{dw}{dy}(y = \pm a, \forall x) &= 0
\end{aligned} \tag{4.11}$$

During the CMUT operation mode, it experiences two types of loads, first is the electrostatic force between the membrane and the back plate, and second is the atmospheric pressure on top of the membrane. So the combined load deflection model for the square clamped multi-layer membrane which includes both electrical and ambient pressure load is expressed as [48]

$$\begin{aligned}
\left[C_s f_s(\nu) \frac{\tilde{E}t}{a^4} \right] w_0^3 + \left[C_r \frac{\sigma_0 t}{a^2} + C_b \frac{12D_{eff}}{a^4} - \frac{\varepsilon_0 V^2}{2a} \left(\frac{4a}{d_{eff}^3} + 0.394 \frac{a^{0.25}}{d_{eff}^{2.25}} \right) \right] w_0 \\
- \left[P_{ext} + \frac{\varepsilon_0 V^2}{2a} \left(\frac{2a}{d_{eff}^2} + 0.315 \frac{a^{0.25}}{d_{eff}^{1.25}} \right) \right]
\end{aligned} \tag{4.12}$$

where w_0 is the diaphragm center deflection, σ_0 is the residual stress in the diaphragm, ε_0 is the permittivity of free space, V is the bias voltage, D_{eff} is the effective flexural rigidity, P_{ext} is the external mechanical pressure, and ν is the Poisson's ratio of the diaphragm material. The term within the first square bracket represents diaphragm stiffness resulting from nonlinear spring hardening, the first term within the second square bracket represents diaphragm stiffness resulting from the residual stress, the second term within the second square bracket represents the diaphragm stiffness resulting from bending, the third term within the second square bracket represents electrostatic spring softening resulting from the bias voltage V , and finally, the second term within the third square bracket represents the linearized electrostatic pressure. The real root of the third-order polynomial (4.12) represents the center deflection of the diaphragm subject to an external pressure and the electrostatic pressure resulting from the bias voltage. Constants C_r , C_b , and C_s , for thin diaphragms are 3.45, 4.06 and 1.994 respectively. The poisson ratio dependent function, $f_s(\nu)$ in 4.12, can be expressed as:

$$f_s(\nu) = \frac{1 - 0.271\nu}{1 - \nu} \tag{4.13}$$

The CMUT membrane discussed here is a multilayer membrane having different physical properties for each of its layers. A multilayer membrane is shown in figure (4.15)

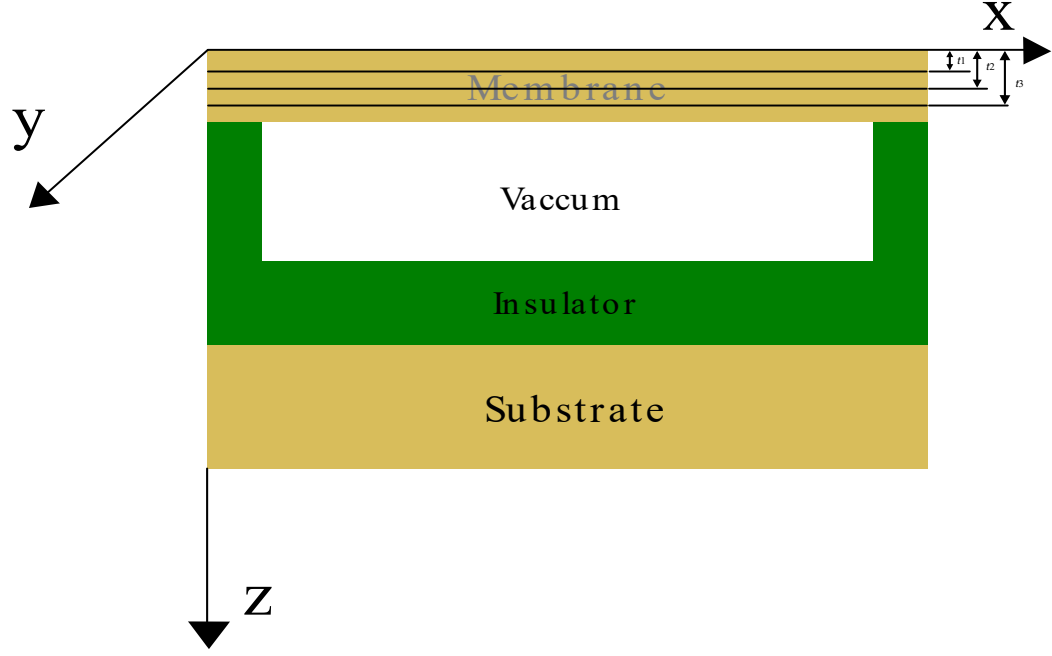


Figure 4.15: Multilayer membrane

Effective flexural rigidity D_{eff} in (4.12), of a multilayer membrane can be expressed as:

$$D_{eff} = \frac{AC - B^2}{A} \quad (4.14)$$

The constants A , B and C , can be expressed as [48]:

$$A = \sum_k Q_k (t_k - t_{k-1}), \quad (4.15)$$

$$B = \sum_k Q_k \left(\frac{t_k^2 - t_{k-1}^2}{2} \right), \quad (4.16)$$

$$C = \sum_k Q_k \left(\frac{t_k^3 - t_{k-1}^3}{3} \right), \quad (4.17)$$

And,

$$Q_k = \frac{E_k}{1 - \nu_k^2} \quad (4.18)$$

where, k denotes the k^{th} layer of the membrane, E_k is the Young's modulus of the membrane layer material and ν_k denotes the poisson's ratio of the particular layer of the membrane. The effective

gap, d_{eff} in (4.12), can be calculated as:

$$d_{eff} = \frac{d_m}{\epsilon_m} + \frac{d_t}{\epsilon_t} + d_0 \quad (4.19)$$

where, d_0 is the gap between the membrane and the backplate, d_m is the membrane thickness, ϵ_m is the dielectric constant of the membrane, d_t is the thickness of the top electrode, and ϵ_t is the dielectric constant of the top electrode. The deflection profile of a multilayer diaphragm can be calculated by:

$$w(x, y) = \left[w_0 + w_1 \left(\frac{x^2 + y^2}{a^2} \right) + w_2 \left(\frac{x^2 y^2}{a^4} \right) + w_3 \left(\frac{x^4 + y^4}{a^4} \right) \right] \cos^2 \left(\frac{\pi x}{2a} \right) \cos^2 \left(\frac{\pi y}{2a} \right) \quad (4.20)$$

Where, w_0 is the deflection of the membrane which can be found from 4.20, and the parameters w_1 , w_2 , and w_3 can be found from:

$$\begin{aligned} w_1 &= \frac{0.0013}{\sqrt{t}} w_0, \\ w_2 &= \frac{0.005}{\sqrt{t}} w_0, \\ w_3 &= \frac{0.0021}{\sqrt{t}} w_0 \end{aligned} \quad (4.21)$$

where t denotes the thickness of the membrane.

All the above mentioned calculation has been done using the material properties and CMUT specifications mentioned in Table 4.4 and 4.5 respectively. Figure 4.16 shows a cross section view of a CMUT

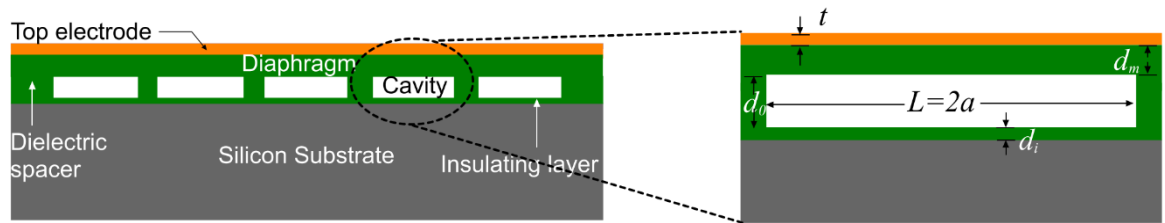


Figure 4.16: CMUT Cross Section [9].

Parameter	Unit	BCB (Diaphragm)	Gold (Top electrode)	Silicon <100> (Substrate)
Density, ρ	kg/m ³	1050	19300	2329
Young's modulus, E	GPa	2.9	70	165
Poisson's ratio, ν		0.34	0.44	0.26
Residual stress, σ	MPa	28	106	55
Relative permittivity, ε		2.6	1	11.8

Table 4.4: Material properties of CMUT cell

Parameter	Unit	Value
Cell sidelength, $L = 2a$	μm	24
Diaphragm thickness, d_m	μm	1.3
Cavity height, d_0	μm	0.4
Top electrode thickness, t	μm	0.1

Table 4.5: Design specification of CMUT cell

Using equations from (4.12) to (4.21), the deflection profile of the CMUT membrane at atmospheric pressure of 101.3 kPa is calculated analytically using MATLAB. The analytical model is then compared with the FEA analysis carried out in Intellisuite and is shown in Figure 4.17 and 4.18

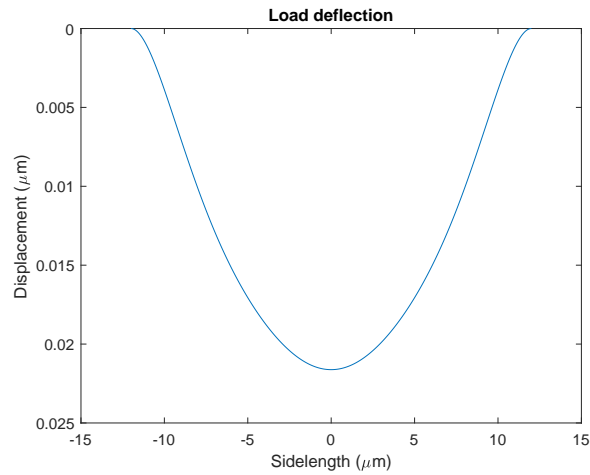


Figure 4.17: Load deflection of the membrane

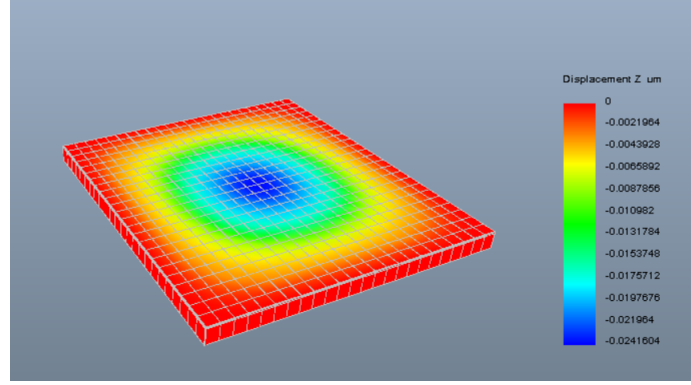


Figure 4.18: Load deflection of the membrane

4.3 Capacitance

The membrane and the bottom electrode separated by the dielectric medium act as a parallel plate capacitor. The total capacitance of the undeformed CMUT membrane can be calculated using [48]:

$$C = C_0(1 + C_{ff}) \quad (4.22)$$

where C_0 is the parallel plate capacitance which can be expressed as:

$$C_0 = \frac{\epsilon_0 4a^2}{d_{eff}} \quad (4.23)$$

And, C_{ff} is the capacitance due to fringing field factor, which can be expressed as:

$$C_{ff} = \frac{0.385d_{eff}}{a} + 1.06 \left(\frac{d_{eff}}{2a} \right)^{0.75} + \frac{0.53}{a} (d_c d_{eff})^{0.5} \quad (4.24)$$

As the membrane deflects towards the bottom electrode due to applied DC bias voltage, the capacitance also changes. The capacitance after deformation of the membrane, C_{deform} can be calculated by modifying the equation (4.22):

$$C = C_{deform}(1 + C_{ff}) \quad (4.25)$$

Also, C_{deform} can be calculated from:

$$C_{deform} = \epsilon_0 \iint_A \left(\frac{dxdy}{d_{eff} - w(x,y)} \right) \quad (4.26)$$

As the diaphragm edges are rigidly fixed and don't undergo any deformation and the fringing field capacitance is contributed mainly by the charges concentrated at the edges, the fringing field factor C_{ff} can be assumed to remain unchanged despite diaphragm deformation [48].

The capacitance of the undeformed CMUT diaphragm is found to be:

Analytical	FEA	% Deviation
3.67 fF	3.47 fF	5.7

Table 4.6: Comparison of capacitance

4.4 Resonant Frequency

Resonant frequency in air has been calculated using the equation [49]:

$$f_{res} = \sqrt{\frac{1}{\rho} \left(\frac{D_{eff}\pi^2}{a^4} + \frac{T}{2a^2} \right)} \quad (4.27)$$

where, $T = \sigma \times t$, is the tensile force and $2a$ is the sidelength of the membrane, and ρ is the density of the membrane material. The analytical calculation has been performed in MATLAB and it is in accordance with the FEA simulation carried out in Intellisuite is shown below:

Analytical	FEA	% Deviation
7.5 MHz	7.2 MHz	4.1

Table 4.7: Comparison of natural frequency

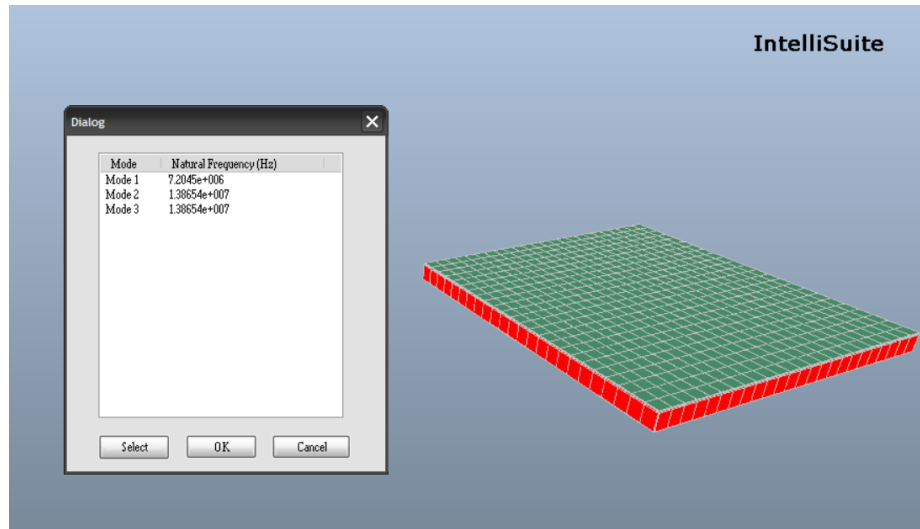


Figure 4.19: Natural frequency FEA simulation

The diaphragm mechanical impedance was calculated by solving the fourth-order differential equation of motion presented in [50] and electrical impedance in the air was calculated by simplifying the first-order equivalent circuit model presented in [50]. The diaphragm mechanical impedance and electrical imaginary impedance are plotted in Figure 4.20 and 4.21, respectively as a function of frequency.

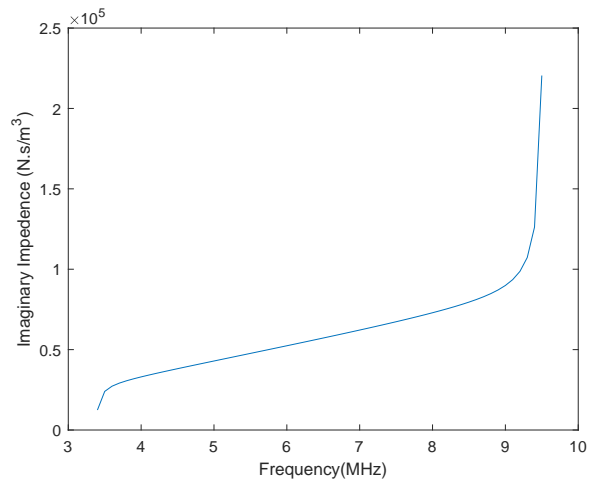


Figure 4.20: Mechanical Impedance

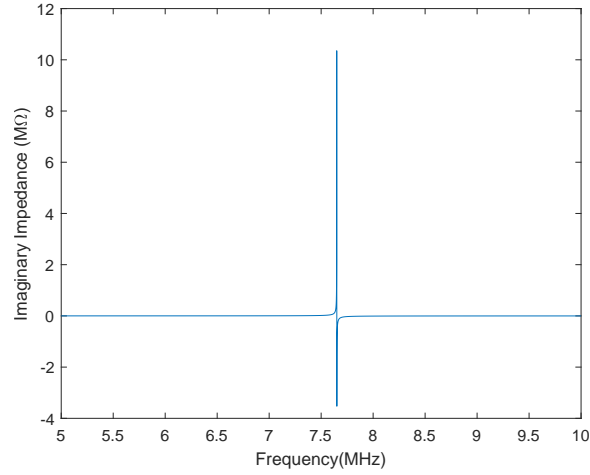


Figure 4.21: Electrical impedance

4.5 Pull-in Voltage

Pull-in voltage is one of the important parameters to design a CMUT array that decides the transmit-receive sensitivity and the dynamic range of the transducer. When biased with a DC voltage, the membrane deflects towards the bottom electrode due to electrostatic attraction force. The mechanical restoring force of the membrane balances this deflection. However, after increasing the bias voltage beyond a certain limit, known as collapse or pull-in voltage, the electrostatic force starts dominating over the restoring force and the membrane collapses over the bottom electrode [8]. The pull-in voltage for an ideal parallel plate electrostatic actuator is:

$$V_{pi} = \sqrt{\frac{8Kd_0^3}{27\varepsilon_0}A} \quad (4.28)$$

where K is the equivalent spring constant, ε_0 is the permittivity of free space, and A is the diaphragm area. But studies have shown Equation 4.28 is not fully accurate in understating the pull-in voltage. So a modified and efficient form of pull-in voltage has been shown in Equation 4.29. Pull-in voltage for a square diaphragm can be calculated from [51]:

$$V_{pi} = \sqrt{\frac{6d_0^2}{5\varepsilon} \left(C_1 \frac{t_d \sigma}{a^2} \left(\frac{d_0}{3} \right) + C_2(\nu) \frac{t_d \tilde{E}}{a^4} \left(\frac{d_0}{3} \right)^3 \right)} \quad (4.29)$$

where $2a$ is the sidelength of the membrane, d_0 is the cavity height. The collapse voltage calculated mathematically using the above equation is 205.5 V.

The coupling coefficient is an important parameter because it characterizes an ultrasonic transducer. Coupling coefficient can be defined as the ratio of the mechanical energy stored to the total electrical energy. Initially, k_T^2 is zero and increases as the displacement increases. When the displacement equals one-third of the initial gap distance, the electrostatic force gradient is larger than that of mechanical force and the top plate collapses on the bottom electrode; at this point k_T^2 is equal to 1. For the CMUT, k_T^2 is calculated using fixed (C_s) and free (C_T) the capacitance of the transducer [52]. Electromechanical coupling coefficient k_T^2 calculated analytically is shown below:

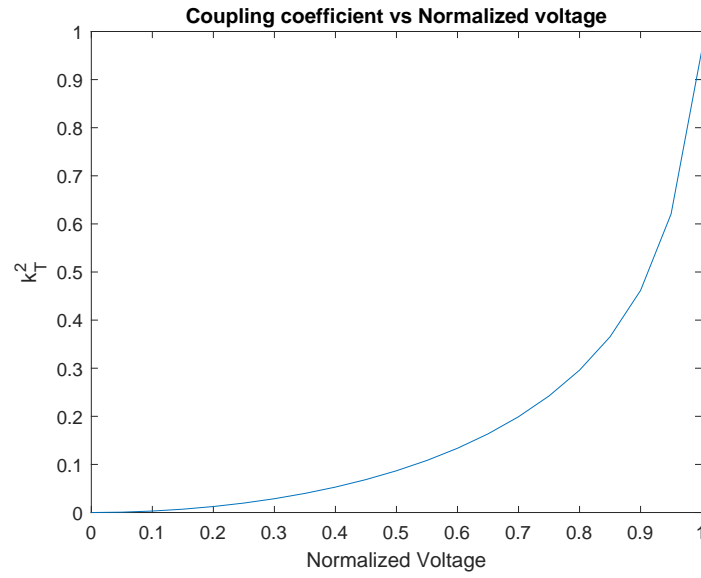


Figure 4.22: Coupling coefficient

Chapter 5

CMUT Dual Mode Operation for diagnosis of Liver fibrosis

5.1 Liver Fibrosis

Liver fibrosis is the excessive accumulation of extracellular matrix (ECM) proteins including collagen that occurs in most types of chronic liver diseases. Advanced liver fibrosis results in cirrhosis, liver failure, and portal hypertension and often requires liver transplantation [53].

Chronic liver injury, irrespective of cause, is generally associated with the accumulation of matrix proteins, a process referred to as fibrosis. In parallel with this, there is a continued stimulus for regeneration, leading to further distortion of the hepatic architecture and vascular structures (portal veins, hepatic veins). This results in a transformation to a nodular architecture, so called cirrhosis [54]. The main causes of liver fibrosis in industrialized countries include chronic HCV infection, alcohol abuse, and nonalcoholic steatohepatitis (NASH). The accumulation of ECM proteins distorts the hepatic architecture by forming a fibrous scar, and the subsequent development of nodules of regenerating hepatocytes defines cirrhosis. Cirrhosis produces hepatocellular dysfunction and increased intrahepatic resistance to blood flow, which result in hepatic insufficiency and portal hypertension, respectively [53]. Figure (5.23) shows condition of liver at different stages of liver disease.

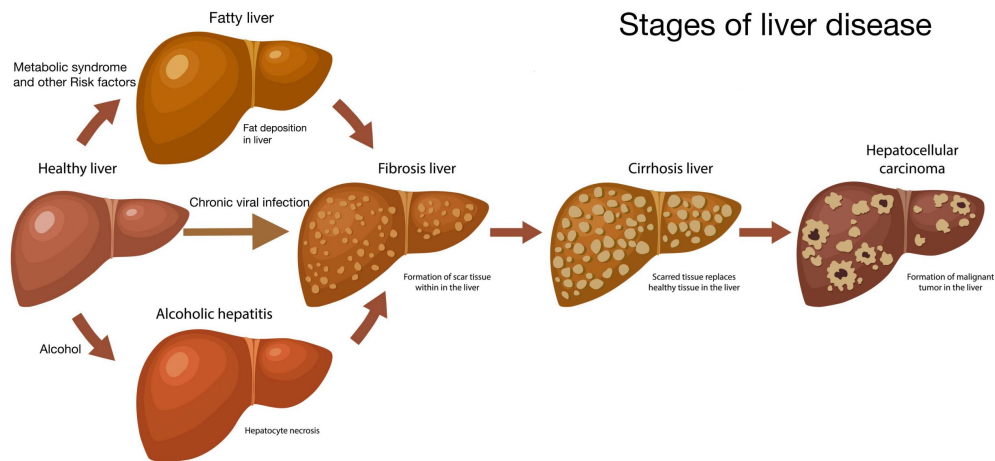


Figure 5.23: Condition of liver at different stages of liver disease [10].

The onset of liver fibrosis is usually insidious, and most of the related morbidity and mortality occurs after the development of cirrhosis. In the majority of patients, progression to cirrhosis occurs after 15–20 years. Major clinical complications of cirrhosis include ascites, renal failure, hepatic encephalopathy, and variceal bleeding. Patients with cirrhosis can remain free of major complications for several years (compensated cirrhosis). Decompensated cirrhosis is associated with short survival, and liver transplantation is often indicated as the only effective therapy. Cirrhosis is also a risk factor for developing hepatocellular carcinoma. Liver fibrosis progresses rapidly to cirrhosis in several clinical settings, including repeated episodes of severe acute alcoholic hepatitis, subfulminant hepatitis, and fibrosing cholestasis in patients with HCV reinfection after liver transplantation [53].

Looking at the severity of liver disease, it is very important for accurate and also early detection, if not, can lead to liver cancer, and then the only option that remains for the patient is a liver transplant. Currently, liver biopsy is considered the gold standard for evaluating hepatic fibrosis which is an invasive and painful procedure that creates a lot of discomfort for the patient who is already suffering from liver disease. There are cases of sampling error that can lead to an incorrect diagnosis. Even when an experienced physician performs liver biopsy and an expert pathologist interprets the results, liver biopsy has up to a 20% error rate in disease staging [14]. So, a non-invasive method is very much needed for accurate measurement of the degree of liver fibrosis. Transient Elastography (TE) is one such method that accurately measures the fibrosis of the liver.

5.2 Transient Elastography

Transient elastography is a non-invasive method for the assessment of hepatic fibrosis in patients with chronic liver diseases, by measuring liver stiffness [14]. Transient elastography differs from other ultrasound (US) based elastographic techniques by the kind of mechanical stimulation it relies on. The use of a transient vibration presents several advantages. First, the transmitted elastic wave can be temporally separated from reflected elastic waves. Thus, the technique is less sensitive to boundary conditions than other elastographic techniques. Second, the acquisition time is short (typically less than 100 ms), which enables measurements to be made on moving organs. Transient elastography is, thus, well adapted to the study of the liver [19]. Pulse-echo ultrasound acquisition is used to follow the propagation of the shear wave and to measure its velocity, which is directly related to tissue stiffness (the elastic modulus E expressed as $E = 3\rho V^2$, where V is the shear velocity and ρ is the mass density (constant for tissues)): the stiffer the tissue, the faster the shear wave propagates [14].

In this thesis, a dual mode CMUT array has been designed which measures fibrosis in the liver using transient elastography technique by generating an image of the liver for proper diagnosis. The two modes in this CMUT works one after the other. First is the high intensity focused ultrasound (HIFU) mode. In this mode, a short high intensity ultrasound wave (shear wave) is directed towards the target region. This high intensity ultrasound wave induces a mechanical disturbance that momentarily disturbs the tissue and then the CMUT is switched to imaging mode where it captures the elastic image of the deformed tissue.

5.3 Dual Mode CMUT

The designed CMUT probe works in two different modes. The details of the two modes are given below.

5.3.1 Mode 1: HIFU

Ultrasound can penetrate deep into tissues and interact with human tissue via thermal and mechanical mechanisms. The ability to focus an ultrasound beam and its energy onto millimeter-sized targets was a significant milestone in the development of therapeutic applications of focused ultrasound. Focused ultrasound can be used as a non-invasive thermal ablation technique for tumor treatment and is being developed as an option to standard oncological therapies. High-intensity focused ultrasound has now been used for clinical treatment of a variety of solid malignant tumors,

including those in the pancreas, liver, kidney, bone, prostate, and breast, as well as uterine fibroids and soft-tissue sarcomas [55]. High intensity focused ultrasound (HIFU) is being promoted as the only completely non-invasive and extracorporeal method to treat primary solid tumors and metastatic disease. The key to HIFU treatment is to deliver the energy required to raise the tissue temperature to a cytotoxic level sufficiently fast such that the tissue vasculature does not have a significant effect on the extent of cell killing.

5.3.1.1 Principles behind HIFU

HIFU produces a focused ultrasound beam that passes through the overlying skin and tissues to necrose a localized region (tumor), which may lie deep within the tissues [55]. But in this thesis, the HIFU has not been used completely from a therapeutic point of view. Here instead of complete ablation of target tissue which generally results in a breakdown of tissue cell structure, the intensity of the HIFU beam has been controlled and a specific amount of acoustic pressure has been directed towards the target tissue. As per FDA guidelines, the amount of acoustic energy sent to the human body must be, is given in table (5.8) [43].

Parameters	Values
ISPTA	<94 mW/cm ²
ISPPA	<190 mW/cm ²

Table 5.8: FDA approved acoustic output exposure levels

5.3.1.2 Pressure field calculation

Proper pressure towards the target point is very much essential for precise and accurate induction of disturbance of the target tissue so that elasticity imaging can be carried out perfectly. So to do this, a correct pressure field calculation is important. The transducer is assumed to be mounted in an infinite, rigid baffle. Enforcing appropriate boundary conditions, the emitted field can be found by solving the wave equation for the velocity potential ψ [56],

$$\nabla^2 \psi - \frac{1}{c_0^2} \frac{\partial^2 \psi}{\partial t^2} = 0 \quad (5.30)$$

And, thus the pressure is calculated as [56]:

$$p_1(\vec{r}, t) = \rho_0 \frac{\partial \psi(\vec{r}, t)}{\partial t} \quad (5.31)$$

While designing the CMUT array, the above parameter has been taken into consideration, and

thus the output pressure at the near field of the transducer surface as well as on the target point has been adjusted. As per [57], it is observed that when 1MPa pressure on the surface of the transducer is achieved then, a successful target tissue ablation is reached at the focus. Following this understanding, simulations have been carried out using different array configurations. The array simulation below has been carried out in FIELD II [56] [58] ultrasound field simulation software.

The figure 5.24 shows the single CMUT cell pressure profile.

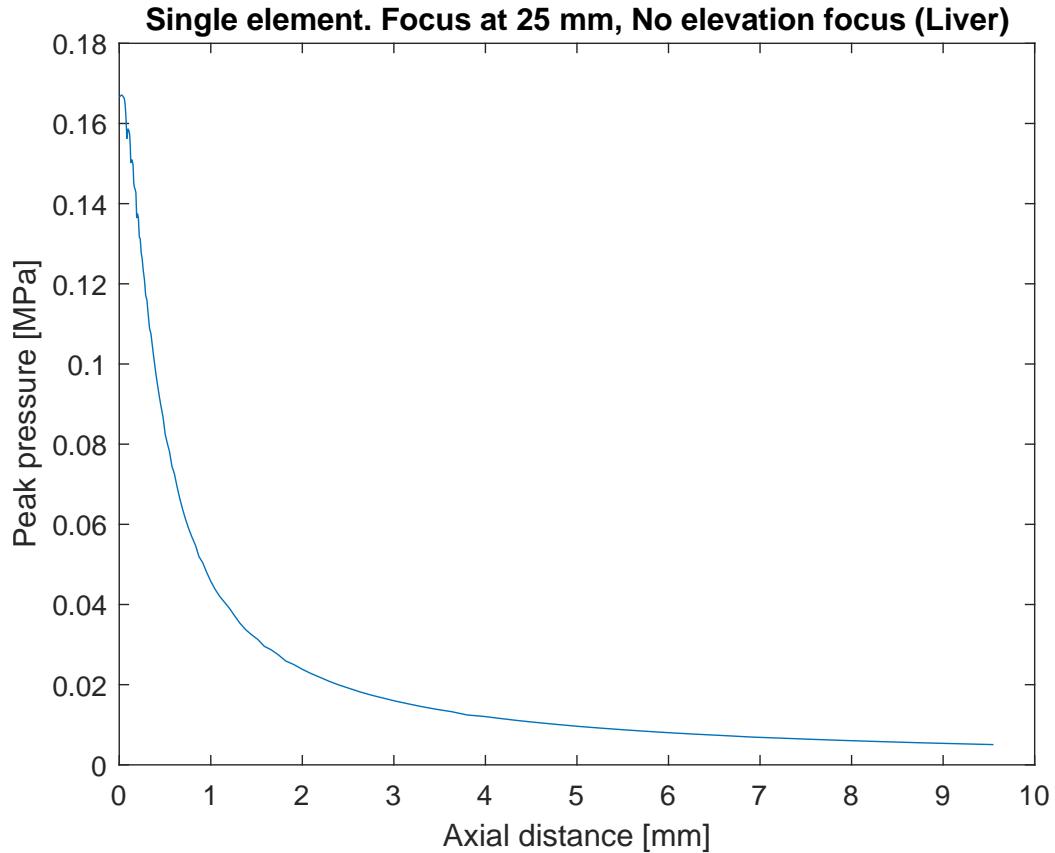


Figure 5.24: Pressure profile for a single CMUT cell

Looking at the above plot, it is clear that a single cell is not able to generate the required amount of pressure for the target tissue. An array of CMUT cells is needed to generate the amount of pressure needed to ablate the target tissue.

In the following figures, it is shown different array configurations and their intensity and pressure profile. The acoustic intensity here used is 25 mW/cm².

- **Intensity and pressure profile for an 8×8 array**

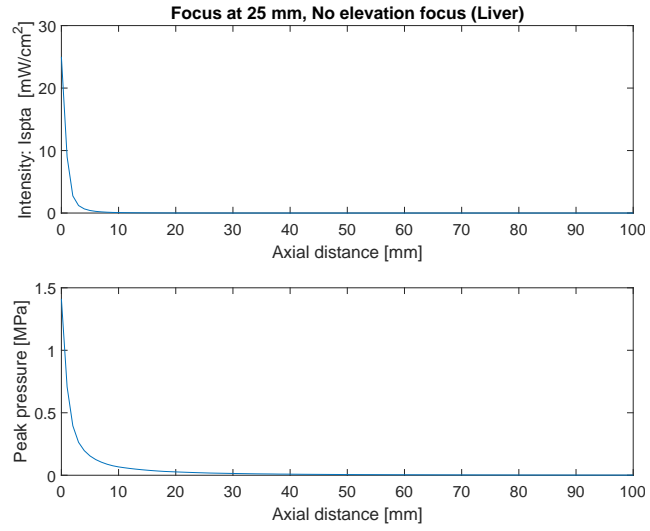


Figure 5.25: Pressure and Intensity profile for 8×8 CMUT array

- Intensity and pressure profile for an 16×16 array

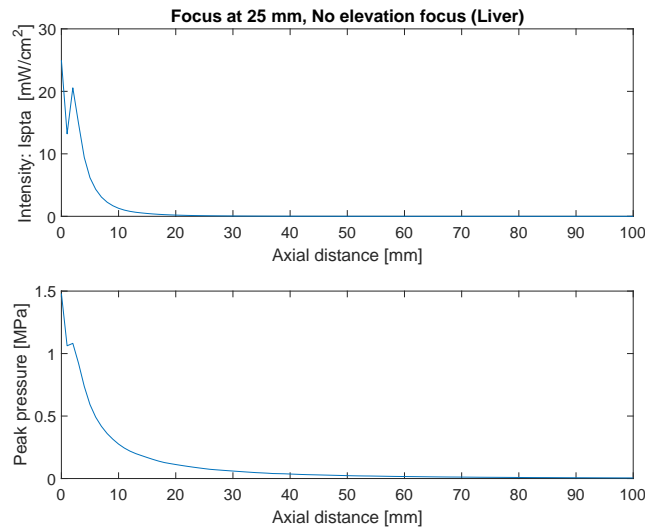


Figure 5.26: Pressure and Intensity profile for 16×16 CMUT array

- Intensity and pressure profile for an 32×32 array

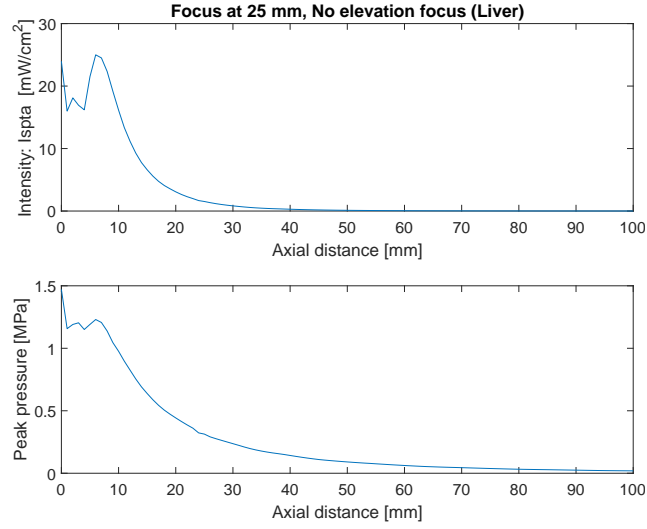


Figure 5.27: Pressure and Intensity profile for 32×32 CMUT array

- **Intensity and pressure profile for an 64×64 array**

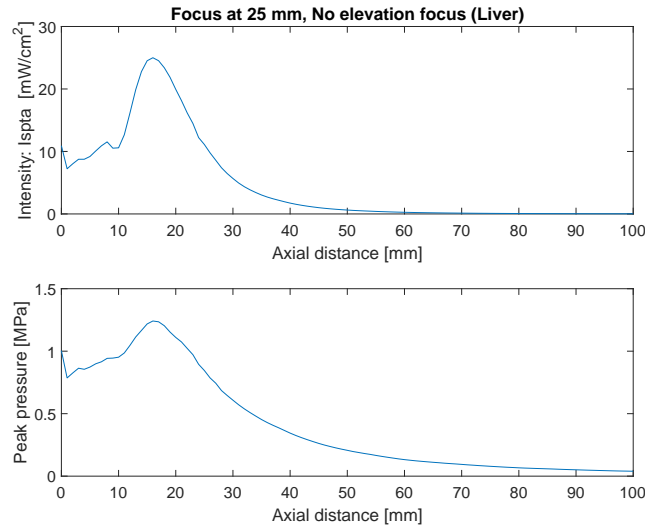


Figure 5.28: Pressure and Intensity profile for 64×64 CMUT array

In the above CMUT array, the focus is set at 25 mm, which is an approximate distance of the liver from the surface of human skin. When ultrasonic pulse travels through a human body, it passes different layers of skin, and also surrounding tissues and blood vessels, thus experiencing acoustic impedance. While simulating with different array configurations for targeted liver tissue, the acoustic impedance has been taken into consideration. Table 5.9 shows acoustic impedance of different tissue.

Tissue	Density (g/cm³)	Speed of sound (m/sec)	Acoustic Impedance [kg/(sec·m²)] × 10⁶
Water	1	1480	1.48
Blood	1.005	1575	1.66
Fat	0.95	1450	1.38
Liver	1.06	1590	1.69
Kidney	1.05	1570	1.65
Brain	1.03	1550	1.60
Heart	1.045	1570	1.64
Muscle (along the fibres)	1.06	1575	1.68
Skin	1.15	1730	1.99
Eye (Lens)	1.04	1650	1.72
Bone axial	1.9	2800	5.32

Table 5.9: Physical properties of different tissue. [2]

In Figures (5.25 to 5.28), pressure profiles on the array surface as well as at the focus is shown. As per [57], the 64×64 array configuration has been chosen according to its near field pressure profile on the array surface. As the array configuration has been chosen, so further calculations and simulations have been done on 64×64 CMUT array.

5.3.2 Mode 2: Imaging

As discussed in the previous section, the 64×64 has been used for imaging the target tissue. Below are a few validations of the array responses.

5.3.2.1 Array performance analysis

A fully working array is very important for the proper image generation of the target. After designing the array, the working of all the elements in the CMUT array needs to be tested. One of the ways to test the response of each of the elements of the array is to test the scattering of point response. The simulation has been done in Field II [56] [58] software.

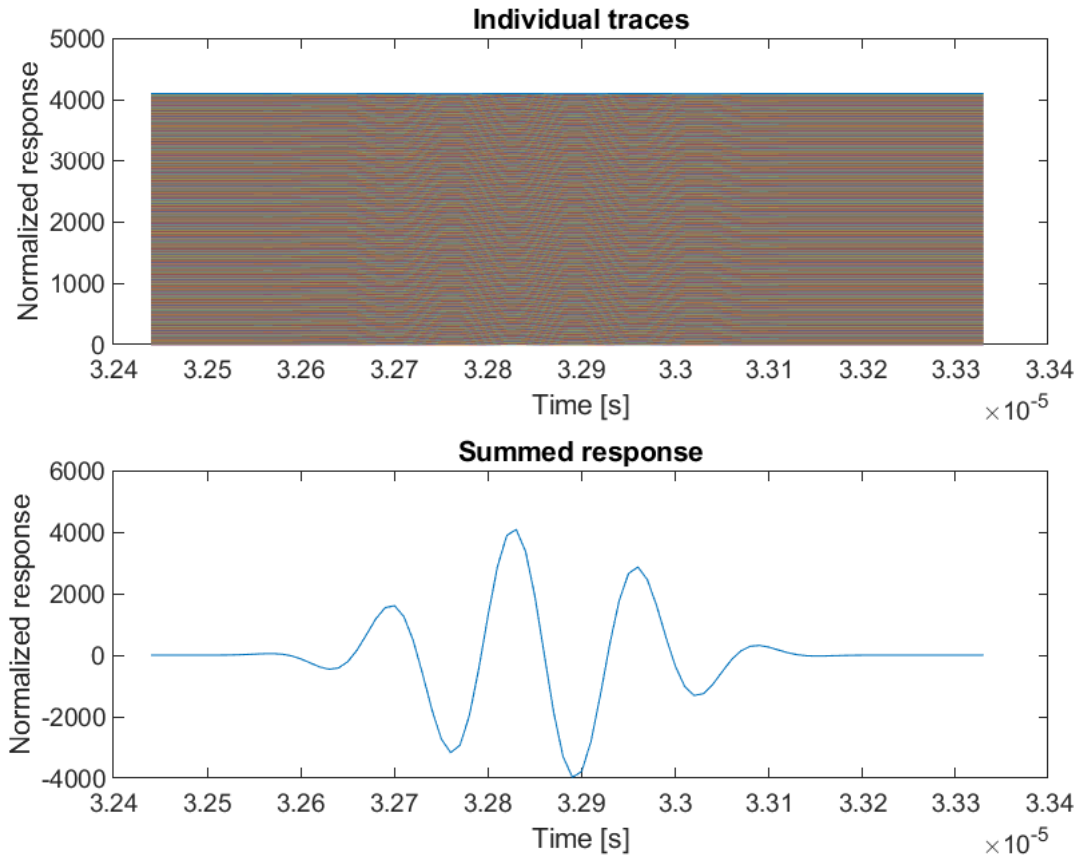


Figure 5.29: Receive voltage traces of point scatter for 64×64 CMUT array

Top plot of the Figure 5.29 shows individual element response traces of each of the elements of the 2D array, whereas the bottom plot represents the sum of all the individual responses. Here all the signal is received at each elements of the 2D array from the collection of scatters placed at 25mm distance from the array surface as phantom points.

Another performance analysis of the 2D array has been carried out in Field II [56] [58] software in the form of pulse-echo field representation of a point object placed at 25 mm from the array surface. As in the simulation environment, it is not possible to move the array physically, so the point is moved from -10mm laterally in an increment of 0.2mm till +10mm at a distance of 25mm to the aperture. Figure 5.30 show the pulse-echo field of a 2D array at a 25mm point object. The envelope of the response is calculated and log compressed to a dynamic range of 60 dB.

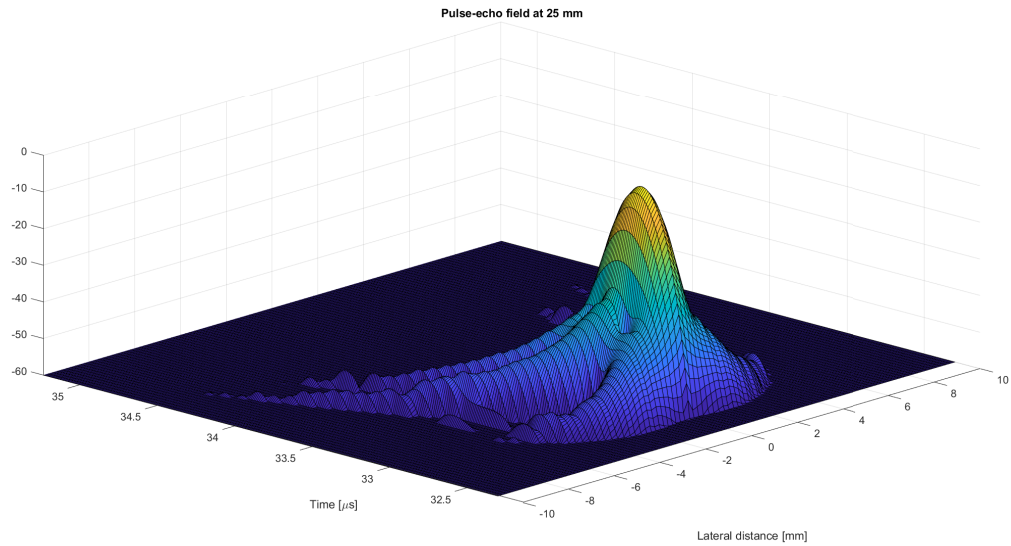


Figure 5.30: Point spread function of the 2D array

5.3.2.2 Phase array imaging of virtual phantom tissues

When the size of the target object is within the aperture of the array, linear array imaging is possible and thus the image can be generated. But when the target object's size is bigger than the imaging array, a linear array imaging system can't capture the entire image. So to overcome this, phase array imaging is used. In phase array imaging the beam is steered all over the image width at a certain angle increment. Figure 5.31 shows two different types of array imaging.

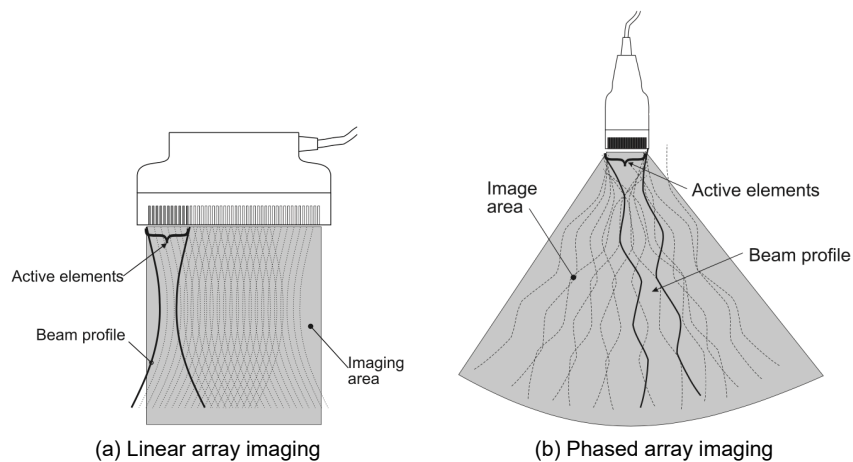


Figure 5.31: Array imaging types [11]

In phase array imaging, the image is sliced in sectors of several RF-lines repeatedly all along the entire width of the image. This method has been used to demonstrate the image generation of two MATLAB generated virtual phantoms that are being used. Both these image generation mentioned below has been done using Field II [56] [58] software. To generate these images, the phantom image is sliced into several RF lines as sectors and the array focus is changed at an increment of a certain angle. Here only 50 RF-lines have been generated as with the present computer setup it would take days to generate a single RF-line for 100,000 scatters, so for this simulation only 2000 scatters have been used. First, is a set of five cyst phantoms [59] whose images have been generated using the above-mentioned process. The phantom contains five-point targets and 6, 5, 4, 3, 2 mm diameter water-filled cysts, and 6, 5, 4, 3, 2 mm diameter high scattering regions. All scatters are situated in a box of $(x,y,z)=(50,10,60)$ mm and the box starts 30 mm from the transducer surface. In the figure 5.32, the white circular spots are the water-filled cysts whose image has been successfully generated. More improved result can be obtained using more scatter points.

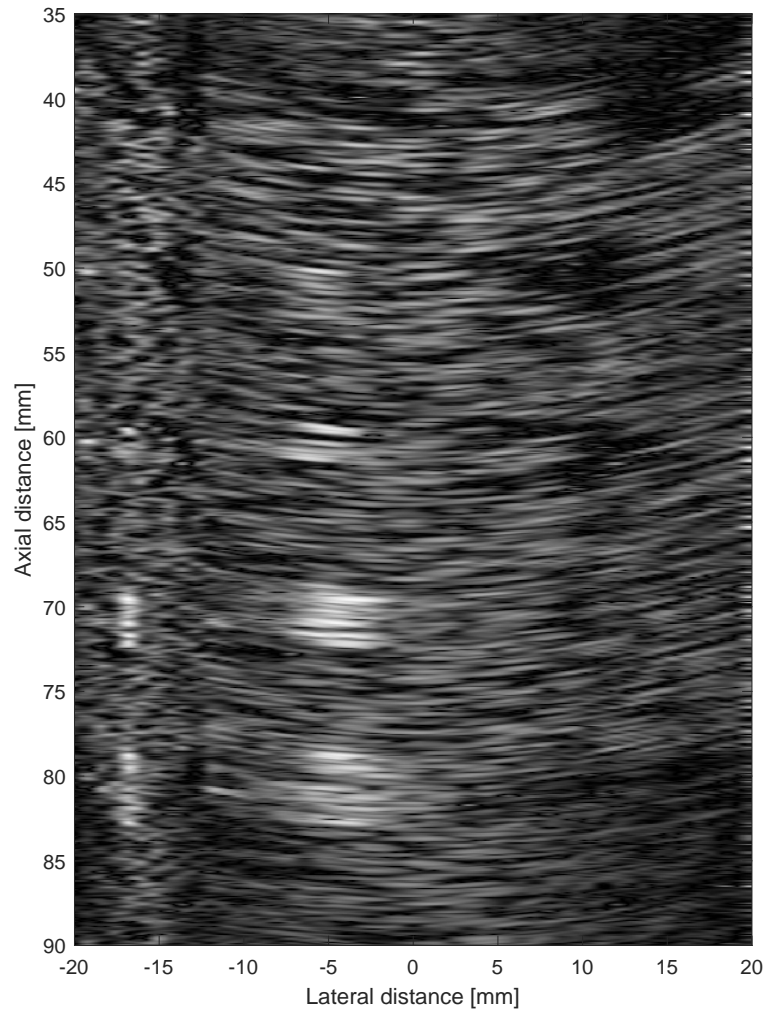


Figure 5.32: Cyst B-mode image

Second image has been generated (figure 5.33) is of a virtual phantom of a fetus. A MATLAB generated virtual phantom for a 3 month old fetus has been used [59]. A transmit focus 70 mm from the transducer was used, and focusing during the reception is at 40 to 140 mm in 10 mm increments. The images consist of 50 lines with 90 degrees between lines.

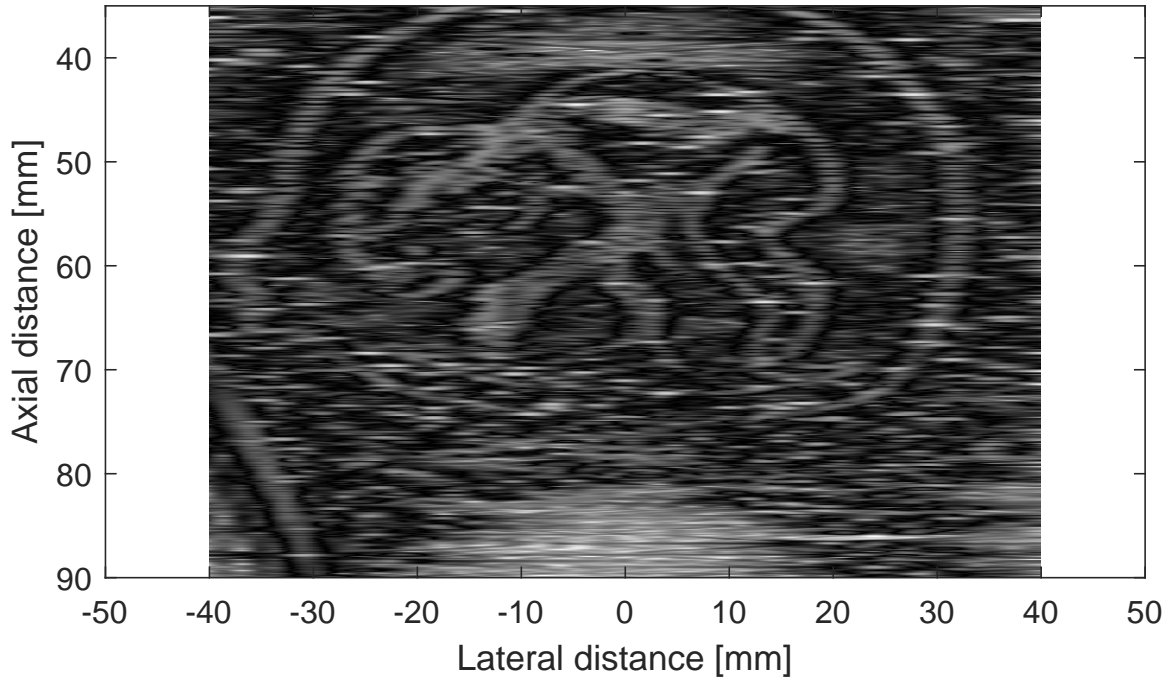


Figure 5.33: Fetus B-mode image

Above two virtual tissue phantoms image has been successfully simulated with the designed array using phased array imaging concept. This proves that the designed array works successfully in imaging mode during simulation. As the above two virtual phantom simulations provides expected results, thus it is also expected that this designed array will also work on real liver tissue as well.

5.4 Elasticity Estimation

RF lines used in the previous section to generate B-mode images of virtual tissue phantoms consist of slices (figure 5.34), which in turn consist of ultrasound scanning lines called A-lines. This method of acquiring the whole volume data at a fixed compression level is necessary to ensure that all the volume slices exhibited the same tissue displacement, and so were consistent with the applied compression level. This facilitated the slices co-registration process, and hence elastography volume construction [12].

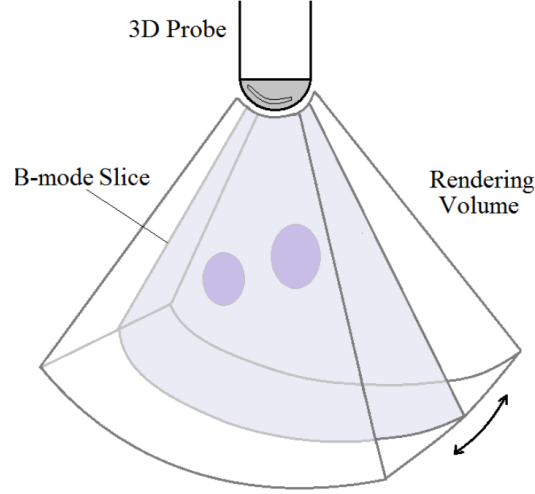


Figure 5.34: Sector imaging with ultrasound probe [12].

After capturing all the RF-lines of B-mode image slice after slice, the total volume is generated using a custom image processing algorithm. Figure 5.35 shows a representation of the entire volume of the image slices.

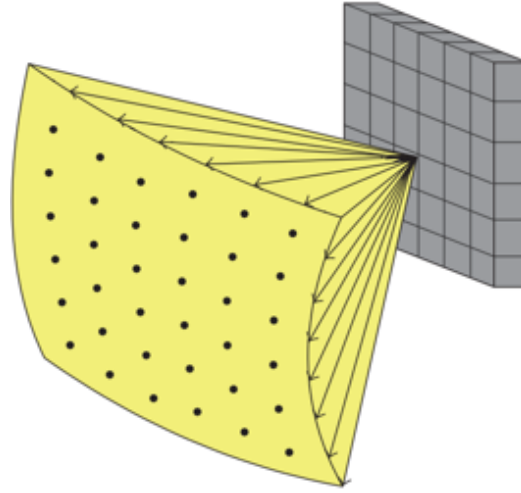


Figure 5.35: Volumetric imaging with 2D array transducer [13]

Elasticity in the medium is derived from the shear velocity. In an isotropic elastic medium, Young's modulus E and the Poisson ratio σ are expressed as [60]

$$E = \frac{\mu(3\lambda + \mu)}{\lambda + \mu} \quad (5.32)$$

$$\sigma = \frac{\lambda}{2(\lambda + \mu)} \quad (5.33)$$

where μ and λ are the Lamé coefficients, respectively, of the shear modulus and bulk modulus.

These equations are valid in soft media if viscosity can be ignored. In soft media, $\lambda \gg \mu$ and, thus, E and σ simplify to

$$E = 3\mu \quad (5.34)$$

$$\sigma = \frac{1}{2} \quad (5.35)$$

The Young modulus only depends on the shear modulus. Because the shear modulus is small, the Poisson ratio is very close to $\frac{1}{2}$. It characterizes the quasi incompressibility of the medium and indicates that shear waves will dominate within the medium. If the medium is purely elastic (dissipation can be ignored), the shear modulus satisfies [60]

$$\mu = \rho V_s^2 \quad (5.36)$$

where V_s is the shear velocity and ρ is the mass density. So from equation 5.34 and 5.36, we get

$$E = 3\rho V_s^2 \quad (5.37)$$

As mass density is known for a tissue, so shear velocity is estimated using linear regression of the evolution of the phase delay of the strain estimates as a function of depth at the center frequency. As long as diffraction effects and dissipation can be ignored, the phase velocity does not differ from the shear velocity that can be expressed as [19]

$$V_s = 2\pi f_0 \left[\frac{\partial \phi(z, f_0)}{\partial z} \right]^{-1} \quad (5.38)$$

where $\phi(z, f_0)$ is the phase delay of the Fourier transform of the strains induced in the medium $\epsilon(z, t)$ and f_0 is the center frequency..

As per [11], to calculate strain estimates, displacement estimation is needed. Displacement estimates are calculated for a tissue using pre and post-compression volumes from RF-lines. Then, normalized cross-correlation was performed between the corresponding pre-compression and post-compression RF windows to produce accurate time delay estimates. Equation 5.39 was used to calculate the normalized cross-correlation function

$$R_{XY} = \frac{\sum_{i=1}^W X(i)Y(i)}{\sqrt{\sum_{i=1}^W X^2(i)}\sqrt{\sum_{i=1}^W Y^2(i)}} \quad (5.39)$$

where R_{XY} is the correlation function, X and Y the pre- and post-compressions RF signals respectively, W is the window length and i an index pointing to the signal samples. The cross correlation

function was calculated at a specified number of time lags between the X and Y signals. And from this estimated displacement is used to calculate tissue strain estimates and its then used in Equation 5.38 to calculate shear velocity and thus we get elasticity of the tissue from equation 5.37.

In the Table 5.10 given below shows the calculation result of liver stiffness at different stages of chronic liver disease. The shear velocity of liver data collected from [14], [19] and [61] uses a low frequency of 50Hz to create deformation in the tissue. Here the mass density ρ , of soft tissue has been considered as 1000 kg/m³.

Elasticity estimation		
Shear velocity (m/s)	Elasticity (kPa)	Fibrosis grade
1.00	3	F0-F1
1.06	3.37	F0-F1
1.60	7.68	F2
1.70	8.67	F2
2.10	13.23	F4
3.00	27	F4
4.80	69.12	F4

Table 5.10: Elasticity estimation and fibrosis grade for chronic liver disease using a low frequency of 50Hz.

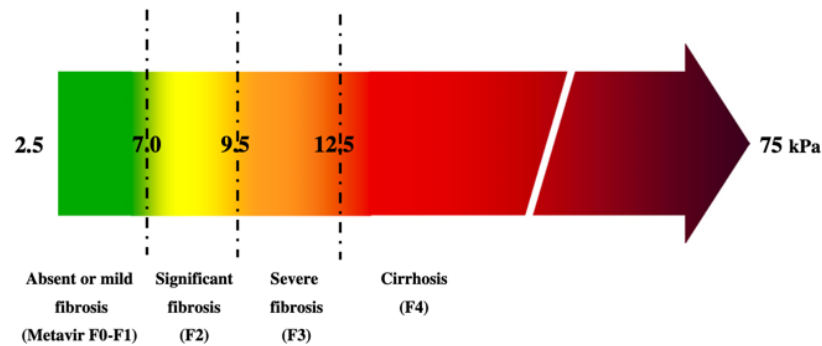


Figure 5.36: Clinical significance of liver stiffness cut-offs in chronic liver diseases. When liver stiffness values range between 2.5 and 7 kPa, mild or absent fibrosis is likely, whereas when liver stiffness values are above 12.5 kPa, cirrhosis is likely. [14]

All the above elasticity estimation in tissue has been calculated using low frequency elastic waves [14], [19] and [61]. It uses two separate devices each for HIFU and imaging. Very few studies has been done using ultrasonic frequency which uses a single transducer for both HIFU and imaging [15]. Table 5.11 shows the comparative data of phase delay of the Fourier transform of strains at tissue depth, induced in the tissue at two different frequencies, 50Hz and 7.5MHz. Shear velocity data from [14], [19] and [61] has been used for calculation.

Shear Velocity (m/s)	Phase delay of the Fourier transform of strain induced in the medium at different centre frequencies	
	At 50Hz	At 7.5 MHz
1.00	314.15	47.1e+6
1.06	296.37	44.4e+6
1.60	196.34	29.4e+6
1.70	184.79	27.7e+6
2.10	149.59	22.4e+6
3.00	104.71	15.7e+6
4.80	65.44	9.8e+6

Table 5.11: Phase delay of the Fourier transform of strain in the medium at 50Hz and 7.5MHz.

From the above Table 5.11, it is observed from the phase delay values that there is a difference of the strains estimates in the target tissue at high frequency compared to low frequency by a factor of 1.49×10^5 .

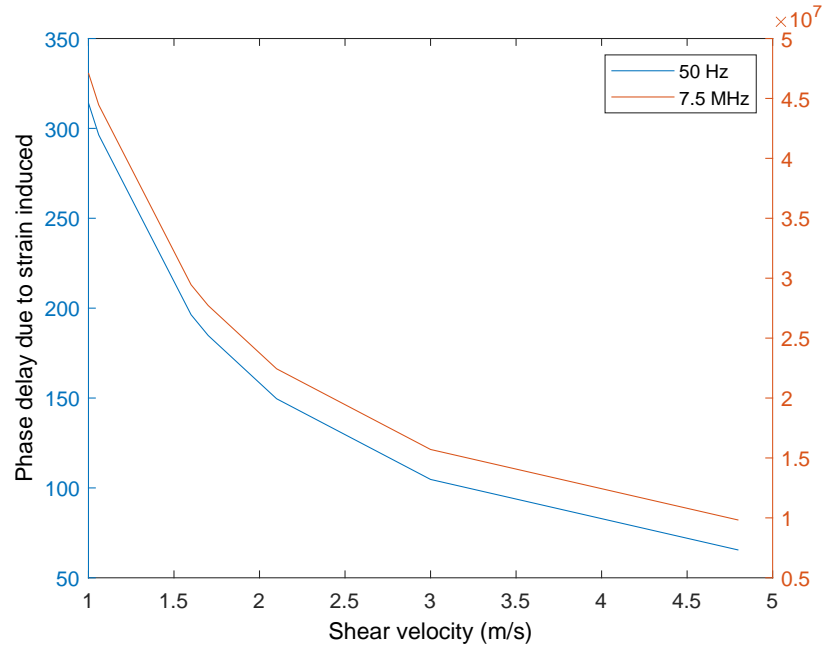


Figure 5.37: Comparative analysis of the phase delay of the Fourier transform of strain in the medium at 50Hz and 7.5MHz frequencies.

Figure 5.37 shows a comparative analysis of the phase delay due to strain in the tissue at corresponding shear velocity.

Calculation of shear velocity and strain in tissue can only be done using a real strain tissue phantom and a complete fabricated transducer array. At present, due to the absence of real tissue phantom and fabricated CMUT probe, it is not possible to calculate the actual data from the designed transducer.

5.5 Switching Circuit

Using a CMUT array in a dual-mode can be challenging, at its operating mode has to change very quickly from HIFU to imaging. Hence, a fast switching circuit is necessary. A high voltage (HV) switch as mentioned in [15] can be used for switching circuit for the designed CMUT array. As mentioned in [15] the pulser in this imaging IC can transmit voltage for HIFU operation, but this would require high power dissipation and would quickly heat the chip. It would be dangerous to use this chip in a clinical setting with patients as it might cause severe burns. Therefore, the HV switch connects the CMUT array to off-chip pulser in HIFU mode. Most of the power consumption in HIFU mode is outsourced to the off-chip pulser, which are not in contact with the patient at the time of the medical procedure. This dual-mode system operates in ultrasound imaging mode and HIFU mode by using the imaging circuits in the IC during imaging mode and off-chip pulser to generate the high-voltage pulse during HIFU.

In this dual-mode IC as mentioned in [15], the pulser excites the CMUT element with a voltage pulse. A delay value is loaded and the global counter frequency is set based on phase delay from each of the transmit elements to the desired focal points. In this way, transmit beamforming is done.

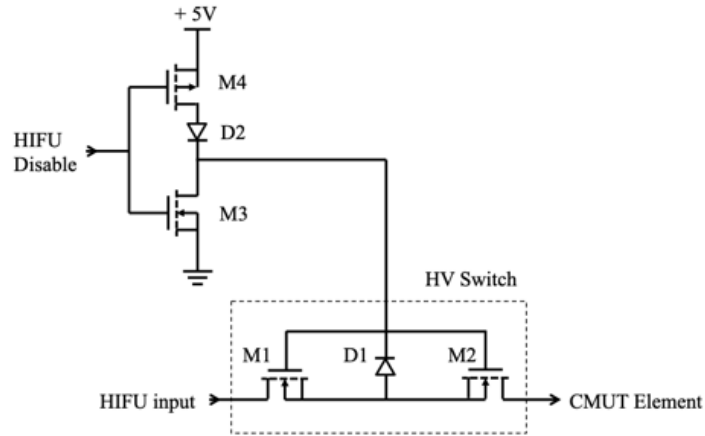


Figure 5.38: Schematics of HV switch [15].

A similar HV switch configuration can be used for the designed CMUT array. In this configuration shown in [15], to enable the switch, the PMOS device (M4) charges the V_{GS} of the HV MOS devices (M1 and M2) to a logic high (5 V), turning on the two devices. Once the two devices M1 and M2 are on, any voltage that is seen at the drain of M1 gets passed on to the output. At this time, there is no current flowing through diode D1 due to the blocking diode D2. The V_{GS} voltages of the two devices are bootstrapped close to 5 V. MOS transistor M3 is off when the switch is enabled. To disable the

switch, the HIFU Disable signal turns on the MOS transistor M3 which starts to discharge the V_{GS} of M1 and M2. At this time, the diode D1 acts like a short bringing the drain and the source of the two transistors to the same potentials.

5.6 Discussion

The elastography imaging mode of the transducer uses multiple RF lines to segment the image and thus create a complete image volume using those slices. During the estimation of tissue deformation, a small segment in the tissue is chosen and the deformed RF lines are analyzed as a function of depth and time and thus the shear velocity is calculated as a function of depth and time.

In [14], [19] and [61] uses low frequency elastic wave to deform the tissue. In the comparative study done in table 5.11 between low-frequency data of 50Hz, and ultrasonic frequency of 7.5MHz of the designed array, it has been found that the data of the phase delay of the Fourier transform of strain in the tissue has a lot of discrepancies, which tells us that there is a difference of strain in the target tissue while using ultrasonic frequency compared to while using low-frequency elastic wave. The analysis shows that at ultrasonic frequency of 7.5 MHz, the generated strain factor deviates from low frequency consistently for different shear velocity by a scale factor of 1.49×10^5 while slope remains almost the same as shown in Figure 5.37. So, if the ultrasonic frequency determined strain factor are calibrated to offset the scale factor, then the low frequency (50 Hz) and ultrasonic frequency (7.5 MHz) determined strain factor would be within $< 1\%$ deviation. The offset error can also be removed by calibration and standardization.

Chapter 6

Conclusion

6.1 Summary

In this research work, a novel technique which has been designed for the first time where it involves a 2D CMUT array that works in a dual-mode wherein mode 1 the CMUT work as HIFU, where it momentarily deforms the target tissue with controlled acoustic intensity and after that, the CMUT is switched to mode 2 which is an imaging mode, where it captures the image of the deformed tissue. Analytical and 3D finite element analysis has been carried out for the CMUT cell showing it is in complete agreement with the design specifications. The main structure of each CMUT cell is of BCB and the top conductor has been used as gold which is placed on top of the diaphragm.

Analysis has been done with different array configurations to find out optimum results for HIFU and imaging. 8×8 , 16×16 , 32×32 and 64×64 , array configurations have been analyzed to get required acoustic pressure on the target, at the same time it has been kept in absolute consideration that the acoustic intensity should not cross the permitted value set by FDA. In the end, 64×64 array configuration has been chosen for the final design. Simulations have been carried out in MATLAB using virtual tissue phantoms. The imaging analysis carried on shows that the array works as expected during imaging mode.

The designed 2D CMUT array work as expected in a simulated environment with virtual tissue phantoms. This design will be of great help in the medical community for the diagnosis of liver cirrhosis at an early stage at a very low cost compared to existing techniques where currently two separate devices have been used for HIFU and imaging purposes.

6.2 Future Works

The dual-mode operation presented in this research has been done for the first time in a 2D CMUT array, thus there is a lot of scope for improvements. As for the scope of this research work is concerned, all the analysis in this research work has been carried on using MATLAB and Intellisuite software and by using virtual tissue phantoms, thus actual tissue deformation data required to calculate the elasticity of the target tissue is not presented and it can only be possible if a real tissue phantom is used with the complete fabricated CMUT array. So an accurate elasticity measurement using the process mentioned in this research work can be obtained with real tissue phantom and a fabricated array.

In this research work, ultrasonic frequency have been used for HIFU. The observed characteristics of strain in the tissue is different in ultrasonic frequency compared to low frequency of 50Hz by a factor of 1.49×10^5 . Thus, further investigation can be carried out for the induced strain in tissue at ultrasonic frequency for calibration and standardization.

This designed CMUT array has application on medical field. So, safety aspect needs to kept in mind. Thermal index is a very important parameter for a transducer in a biomedical application. As this CMUT will be used for detection of liver cirrhosis so its thermal index need to be investigated for its safe use.

Also during the imaging mode, while simulating in MATLAB environment, the computing power of the system used, only allowed to use 2,000 scatter points at the target tissue for generating images presented in a possible time frame. Thus with an industry standard computing power and with more scatter points of around 200,000, a better image result can be obtained.

The scope of this research work was to create a 2D CMUT array for dual-mode operation. So, for the dual-mode to work seamlessly, a fast switching mechanism is needed. A brief investigation on switching circuits has been done and presented in this work. But there is a lot of scope for improvements in designing a much effective and robust switching circuit that can help this CMUT array to switch fast from mode 1 to mode 2.

This research work is focused on designing the array for dual-mode operation. Analysis has been done in the MATLAB environment only. Fabrication and experimental analysis of the CMUT array will add further value to the array technique. Fabrication can be done using low-temperature adhesive bonding of two partially cured wafers and then depositing of gold as top conductor.

Appendix: MATLAB Codes

```
1 %% Bias Voltage
2 clc;
3 close all;
4 clear all;
5 eO=8.85e-12; %Permittivity
6 a=24e-6; %Sidelength
7 td=1.3e-6; %Diaphragm thickness
8 de=0.4e-6+ (td/2.6)+((0.1e-6)/1); %Effective Airgap
9 tb=td; %plate thickness
10 v=0.34; %Poisson ratio
11 E=2.9e9; %Young's modulus
12 Cl=3.45;
13 C2=1.994*(1-0.271*v)/(1-v);
14 Eeff=E/(1-v^2);
15
16 Vpi_1=sqrt((6*de^2/(5*eO))*((Cl*td*sig0/(a/2)^2)*de/3+C2*td*Eeff/(a/2)
    ^4*(de/3)^3));
17
18
19 %% Calculation of load deflection model
20
21 % Initial Variables
22 Cr = 3.45;
23 Cb = 4.06;
24 Cs = 1.994;
```

```

25 v = 0.34; % Poission's ratio of the membrane material
26 a = 24e-6; % Sidelength
27 a_half = a/2; % Half the sidelength
28 dc = 0.1e-06; % Thickness of the conductor
29 t = 1.4e-06; % Membrane thickness
30 sig0 = 28e6; % Residual stress
31 e0 = 8.854e-12; % Permittivity of free space
32 V = 0; % Bias voltage
33 E = 2.9e9; % Young's modulus of the membrane material
34 E_bar = E/(1-v^2);
35 f_v = (1-(0.271*v))/(1-v); % Poisson's ratio dependant function
36 Pext = 101.3e3; % External mechanical pressure;
37
38 % Calcuation of Effective airgap
39 d=0.40e-6; %initial gap
40 dt1=0.1e-6;
41 dt2=1.3e-6;
42 eR1 = 1;
43 eR2 = 2.6;
44 % E=0.79e11;
45 deff=d+(dt1/eR1)+(dt2/eR2);
46
47 % CAlculation of Effective flextural rigidity
48 % Layer 1 Gold
49
50 v1 = 0.44; % Poisson's ratio for layer 1
51 E1 = 70e9; % Young's modulus for layer 1 in GPa
52 t1 = 0.1e-6; % Thickness of layer 1
53 rho1 = 19300; % density for layer 1 in Kg/cm^3
54 sig1 = 106e6; % residual stress for layer 1 in MPa
55 Q1 = E1/(1-(v1)^2);
56
57 % Layer 2 BCB

```



```

58
59 v2 = 0.34; % Poisson's ratio for layer 1
60 E2 = 2.9e9; % Young's modulus for layer 2 in GPa
61 t2 = 1.3e-06; % Total thickness including layer 1
62 rho2 = 1050; % density for layer 2 in Kg/cm^3
63 sig2 = 28e6; % residual stress for layer 2 in MPa
64 Q2 = E2/(1-(v2)^2);
65 rho = rho2*t2;
66
67 T = (t2)*(sig2); % Tensile stress
68 A = (Q1*t1)+(Q2*(t2-t1));
69 B = (Q1*((t1)^2)/2)+(Q2*((t2)^2-(t1)^2)/2);
70 C = (Q1*((t1)^3)/3)+(Q2*((t2)^3-(t1)^3)/3);
71
72 Deff = ((A*C)-B^2)/A;
73
74
75 Vdc=0*Vpi_1;
76 Patm=101325;
77 p1 = (Cs*f_v*E_bar*t2/a_half^4);
78 p2 = ((Cr*sig2*t2/a_half^2)+(Cb*12*Deff/a_half^4)-((e0*Vdc^2/2*a_half)
      *((4*a_half/deff^3)+(0.197*a_half^0.25/deff^2.25))));
79 p3 = Patm + (e0*Vdc^2/2*a_half)*((a_half/deff^2)+(0.1576*a_half^0.25/
      deff^1.25));
80
81 p=[p1 0 p2 -p3];
82 X=roots(p);
83 % P=w_1(real(w_1)>0&imag(w_1)==0);
84 for i=1:3
85     if (X(i)<1/3*deff)
86         w0=X(i);
87     end
88     i=i+1;

```

```

89 end
90 w0
91 w1 = 0.0013*w0/sqrt(t2);
92 w2 = 0.005*w0/sqrt(t2);
93 w3 = 0.0021*w0/sqrt(t2);
94 y = -a_half:0.01e-6:a_half;
95 n = size(y);
96
97 % Deflection shape function
98
99 for j=n(1):n(2)
100     x=0;
101     w(j) = (w0 + (w1*(x^2+y(j)^2)/a_half^2)+ (w2*(x^2*y(j)^2)/a_half^4)+
              (w3*(x^4+y(j)^4)/a_half^4))*cos(pi*x/(2*a_half))^2*cos(pi*y(j)
              /(2*a_half))^2;
102     j = j+1;
103 end
104
105 figure()
106
107 plot(y/1e-6,(w)/1e-6)
108 set(gca, 'Ydir', 'reverse')
109 xlabel('Elevation (\mum)');
110 ylabel('Displacement (\mum)');
111 title('Load deflection');
112
113 %% Capacitance calculation
114 Cff = (0.385*deff/a_half)+(1.06*(deff/(2*a_half))^0.75)+((0.53/a_half)*(
        dc*deff)^0.5);
115 fun= @(x,y) e0./( deff -((w0 + w1*(x.^2 + y.^2)./a^2 + w2* ((x.^2).*y.^2)
        ./a^4 + w3 * (x.^4+y.^4)./a^4)).* ((cos((pi*x)./(2*a))).^2).* (cos((
        pi*y)./(2*a))).^2);
116 C0=integral2(fun,0,a,0,a);

```

```

117 Ctot = C0*(1+Cff);
118
119 %% Coupling coefficeint
120 M=pi^4*rho2*t2*(2*pi^2*Deff + a^2*T)/(64*T);
121 K=2*pi*f_res^2*M*2*pi;
122 n = 1;
123 b = 0; % Damping factor
124 L = M./n^2;
125 C = (n^2)./K;
126 R = b./n^2;
127 w=10e6:10000:18e9;
128 f_2=3.4e6:10e4:9.5e6;
129 w_2=2*pi*f_2;
130 c = ((E2 + sig2)*t2^2)/(12*rho2*(1-v2^2));
131 d_1 = sig2/rho2;
132 k1 = sqrt((sqrt((d_1).^2+(4*c*w_2.^2))-d_1)/(2*c));
133 k2 = sqrt((sqrt((d_1).^2+(4*c*w_2.^2))+d_1)/(2*c));
134 j = sqrt(-1);
135 V=(0:0.05:1)*Vpi_1; %range of bias voltage
136 A = a*a;
137 k=(16*E*a.*t^3)/(L^3); %spring constant for a center loaded fixed-fixed
    beam
138 for t=1:21 % variable for matrix index
139 P_1=e0*A*V(t)^2/(2*k);
140 p_1=[1 -2*deff deff^2 -P_1];
141 X_1=roots(p_1); %cal displacement from third order eqn
142 for i=1:3
143     if(X_1(i)<1/3*deff)
144         d(t)=X_1(i);
145     end
146     i=i+1;
147 end
148 kt_sq(t)=2*d(t)/(deff-d(t)); %calculatin kt^2

```

```

149 d(t) = kt_sq(t)/(deff*(2-kt_sq(t)));
150 t=t+1;
151 end
152
153 figure()
154 plot(V/Vpi_1,kt_sq)
155 xlabel('Normalized Voltage');
156 ylabel('k_T^2');
157 title('Coupling coefficient vs Normalised voltage');
158
159 %% Calculation of Mechanical Impedance
160 Z1= (k2.* besselj(0,k1*a)).* besseli(1,k2*a) + (k1.* besselj(1,k1*a)).*
    besseli(0,k2*a);
161 Z2= 2*((k1.^2)+(k2.^2)).* besselj(1,k1*a)).* besseli(1,k1*a);
162 Zm=j * (((rho2*t2*w_2).*(a*k1)).*k2).*Z1)./(((a*k1).*k2).*Z1-Z2);
163 figure ()
164 plot(f_2*1e-6,imag(Zm));
165 xlabel('Frequency(MHz)');
166 ylabel('Imaginary Impedance (N.s/m^3)');
167
168 %% Calculation of Electrical Impedance
169
170 f=5e6:1000:10e6;
171 w_rad=2*pi*f;
172 Ctot = 3.67e-15;
173 Zp = 1./(j*w_rad*Ctot);
174 Zs= R + (j*w_rad*L) + 1./(j*w_rad*C);
175 Z = (Zp+Zs)./(Zp.*Zs);
176 figure ()
177 plot(f*1e-6,imag(Z)/10e6);
178 xlabel('Frequency(MHz)');
179 ylabel('Imaginary Impedance (M\Omega)');
180 print -depsc elec_impedance.eps

```

```

1  clc;
2
3  close all;
4
5  clear all;
6
7  eO=8.85e-12; %Permittivity
8
9  a=24e-6; %Sidelength
10
11 td=1.3e-6; %Diaphragm thickness
12
13 dg=0.4e-6+ (td/2.6)+((0.1e-6)/1); %Effective Airgap
14
15 tb=td; %plate thickness
16
17 v=0.34; %Poisson ratio
18
19 E=2.9e9; %Young's modulus
20
21 resStress=28e6; %Residual stress
22
23 Cl=3.45;
24
25 C2=1.994*(1-0.271*v)/(1-v);
26
27 Eeff=E/(1-v^2);
28
29
30 Vpi_1=sqrt((6*dg^2/(5*eO))* (...
31
32 (Cl*td*resStress/(a/2)^2)*dg/3 ...
33

```

```

34 +C2*td*Eeff/(a/2)^4*(dg/3)^3));
35
36
37
38 %% Calculation of load deflection model
39
40
41 % Initial Variables
42
43 Cr = 3.45;
44
45 Cb = 4.06;
46
47 Cs = 1.994;
48
49 v = 0.34; % Poission 's ratio of the membrane material
50
51 a = 24e-6;      % Sidelength
52
53 a_half = a/2; % Half the sidelength
54
55 dc = 0.1e-06; % Thickness of the conductor
56
57 t = 1.4e-06; % Membrane thickness
58
59 sig0 = 28e6; % Residual stress
60
61 e0 = 8.854e-12; % Permittivity of free space
62
63 V = 0; % Bias voltage
64
65 E = 2.9e9; % Young 's modulus of the membrane material
66

```

```

67 E_bar = E/(1-v^2);
68
69 f_v = (1-(0.271*v))/(1-v); % Poisson's ratio dependant function
70
71 Pext = 101.3e3; % External mechanical pressure;
72
73
74 % Calculation of Effective airgap
75
76 d=0.40e-6; %initial gap
77
78 dt1=0.1e-6;
79
80 dt2=1.3e-6;
81
82 eR1 = 1;
83
84 eR2 = 2.6;
85
86 % E=0.79e11;
87
88 deff=d+(dt1/eR1)+(dt2/eR2);
89
90
91 % Calculation of Effective flextural rigidity
92
93 % Layer 1 Gold
94
95
96 v1 = 0.44; % Poisson's ratio for layer 1
97
98 E1 = 70e9; % Young's modulus for layer 1 in GPa
99

```

```

100 t1 = 0.1e-6;    % Thickness of layer 1
101
102 rho1 = 19300;    % density for layer 1 in Kg/cm^3
103
104 sig1 = 106e6;    % residual stress for layer 1 in MPa
105
106 Q1 = E1/(1-(v1)^2);
107
108
109 % Layer 2 BCB
110
111
112 v2 = 0.34;    % Poisson's ratio for layer 1
113
114 E2 = 2.9e9; % Young's modulus for layer 2 in GPa
115
116 t2 = 1.3e-06; % Total thickness including layer 1
117
118 rho2 = 1050;    % density for layer 2 in Kg/cm^3
119
120 sig2 = 28e6;    % residual stress for layer 2 in MPa
121
122 Q2 = E2/(1-(v2)^2);
123
124 rho = rho2*t2;
125
126
127 T = (t2)*(sig2); % Tensile stress
128
129 A = (Q1*t1)+(Q2*(t2-t1));
130
131 B = (Q1*(((t1)^2)/2))+(Q2*(((t2)^2-(t1)^2)/2));
132

```



```

133 C = (Q1*(((t1)^3)/3))+(Q2*((t2)^3-(t1)^3)/3);
134
135
136 Deff = ((A*C)-B^2)/A;
137
138
139
140 Vdc=0*Vpi_1;
141
142 Patm=101325;
143
144 p1 = (Cs*f_v*E_bar*t2/a_half^4);
145
146 p2 = ((Cr*sig2*t2/a_half^2)+(Cb*12*Deff/a_half^4)-((e0*Vdc^2/2*a_half)
      *((4*a_half/deff^3)+(0.197*a_half^0.25/deff^2.25)))));
147
148 p3 = Patm + (e0*Vdc^2/2*a_half)*((a_half/deff^2)+(0.1576*a_half^0.25/
      deff^1.25));
149
150
151 p=[p1 0 p2 -p3];
152
153 X=roots(p);
154
155 % P=w_1(real(w_1)>0&imag(w_1)==0);
156
157 for i=1:3
158
159 if (X(i)<1/3*deff)
160
161 w0=X(i);
162
163 end

```

```

164
165 i=i+1;
166
167 end
168
169 w0
170
171 w1 = 0.0013*w0/sqrt(t2);
172
173 w2 = 0.005*w0/sqrt(t2);
174
175 w3 = 0.0021*w0/sqrt(t2);
176
177 y = -a_half:0.01e-6:a_half;
178
179 n = size(y);
180
181
182 % Deflection shape function
183
184
185 for j=n(1):n(2)
186
187 x=0;
188
189 w(j) = (w0 + (w1*(x^2+y(j)^2)/a_half^2)+ (w2*(x^2*y(j)^2)/a_half^4)+ (w3
        *(x^4+y(j)^4)/a_half^4))*cos(pi*x/(2*a_half))^2*cos(pi*y(j)/(2*
        a_half))^2;
190
191 j = j+1;
192
193 end
194

```

```

195
196 figure ()
197
198
199 plot(y/1e-6,(w)/1e-6)
200
201 set(gca, 'Ydir', 'reverse')
202
203 xlabel('Elevation (\mum)');
204
205 ylabel('Displacement (\mum)');
206
207 title('Load deflection');
208
209
210 %% Capacitance calculation
211
212 Cff = (0.385*deff/a_half)+(1.06*(deff/(2*a_half))^0.75)+((0.53/a_half)*(
    dc*deff)^0.5);
213
214 fun= @(x,y) e0./( deff -((w0 + w1*(x.^2 + y.^2)./a^2 + w2* ((x.^2).*y.^2)
    ./a^4 + w3 * (x.^4+y.^4)./a^4)).* ((cos((pi*x)/(2*a))).^2).* (cos((
    pi*y)/(2*a))).^2);
215
216 C0=integral2(fun,0,a,0,a);
217
218 Ctot = C0*(1+Cff);
219
220
221 %% Coupling coefficeint
222
223 M=pi^4*rho2*t2*(2*pi^2*Deff + a^2*T)/(64*T);
224

```

```

225 K=2*pi*f_res^2*M*2*pi;
226
227 n = 1;
228
229 b = 0; % Damping factor
230
231 L = M./n^2;
232
233 C = (n^2)./K;
234
235 R = b./n^2;
236
237 w=10e6:10000:18e9;
238
239 f_2=3.4e6:10e4:9.5e6;
240
241 w_2=2*pi*f_2;
242
243 c = ((E2 + sig2)*t2^2)/(12*rho2*(1-v2^2));
244
245 d_1 = sig2/rho2;
246
247 k1 = sqrt((sqrt((d_1).^2+(4*c*w_2.^2))-d_1)/(2*c));
248
249 k2 = sqrt((sqrt((d_1).^2+(4*c*w_2.^2))+d_1)/(2*c));
250
251 j = sqrt(-1);
252
253 V=(0:0.05:1)*Vpi_1; %range of bias voltage
254
255 A = a*a;
256

```

```

257 k=(16*E*a.*t^3)/(L^3); %spring constant for a center loaded fixed-fixed
    beam
258
259 for t=1:21 % variable for matrix index
260
261 P_1=e0*A*V(t)^2/(2*k);
262
263 p_1=[1 -2*deff deff^2 -P_1];
264
265 X_1=roots(p_1); %cal displacement from third order eqn
266
267 for i=1:3
268
269 if (X_1(i)<1/3*deff)
270
271 d(t)=X_1(i);
272
273 end
274
275 i=i+1;
276
277 end
278
279 kt_sq(t)=2*d(t)/(deff-d(t)); %calculatin kt^2
280
281 d(t) = kt_sq(t)/(deff*(2-kt_sq(t)));
282
283 t=t+1;
284
285 end
286
287
288 figure()

```

```

289
290 plot(V/Vpi_1 , kt_sq)
291
292 xlabel( 'Normalized Voltage ');
293
294 ylabel( 'k_T^2 ');
295
296 title( 'Coupling coefficient vs Normalised voltage ');
297
298
299 %% Calculation of Mechanical Impedance
300
301 Z1= (k2.* besselj(0,k1*a)).* besseli(1,k2*a) + (k1.* besselj(1,k1*a)).*
    besseli(0,k2*a);
302
303 Z2= 2*(((k1.^2)+(k2.^2)).* besselj(1,k1*a)).* besseli(1,k1*a);
304
305 Zm=j * (((rho2*t2*w_2).*(a*k1)).*k2).*Z1) ./ (((a*k1).*k2).*Z1-Z2);
306
307 figure ()
308
309 plot(f_2*1e-6,imag(Zm));
310
311 xlabel( 'Frequency(MHz) ');
312
313 ylabel( 'Imaginary Impedence (N.s/m^3) ');
314
315
316 %% Calculation of Electrical Impedance
317
318
319 f=5e6:1000:10e6;
320

```

```

321 w_rad=2*pi*f;
322
323 Ctot = 3.67e-15;
324
325 Zp = 1./(j*w_rad*Ctot);
326
327 Zs= R + (j*w_rad*L) + 1./(j*w_rad*C);
328
329 Z = (Zp+Zs)./(Zp.*Zs);
330
331 figure ()
332
333 plot(f*1e-6,imag(Z)/10e6);
334
335 xlabel( 'Frequency(MHz) ');
336
337 ylabel( 'Imaginary Impedance (M\Omega) ');
338
339 print -depsc elec_impedance.eps

```

References

- [1] Sumeet K. Asrani, Harshad Devarbhavi, John Eaton, and Patrick S. Kamath. Burden of liver diseases in the world. *Journal of Hepatology*, 70(1):151–171, January 2019.
- [2] Appendix a: Typical acoustic properties of tissues. In *Basics of Biomedical Ultrasound for Engineers*, pages 313–314. John Wiley & Sons, Inc., April 2010.
- [3] "NIDDK". Stage of liver damage high, 2019.
- [4] James Ross McLaughlan. Diagram showing liver lesioning using a hifu transducer.
- [5] Jin Young Kwak and Eun-Kyung Kim. Ultrasound elastography for thyroid nodules: recent advances. *Ultrasonography*, 33(2):75–82, February 2014.
- [6] The Royal Australian College of General Practitioners. Fibroscan and transient elastography.
- [7] Lester W. Schmerr. *Fundamentals of Ultrasonic Phased Arrays*. Springer International Publishing, 2015.
- [8] Rayyan Manwar. "A BCB Diaphragm Based Adhesive Wafer Bonded CMUT Probe for Biomedical Application", Electronic Theses and Dissertations, 5996.
- [9] Varshitha Yashvanth. "CMUT Crosstalk Reduction Using Crosslinked Silica Aerogel", Electronic Theses and Dissertations, 7427.
- [10] knowntreatment.com. Stages of liver disease.
- [11] Jørgen A. Jensen. Ultrasound imaging and its modeling. In *Topics in Applied Physics*, pages 135–166. Springer Berlin Heidelberg.
- [12] Sayed Ahmed A Hameed. *Novel 3D Ultrasound Elastography Techniques for In Vivo Breast Tumor Imaging and Nonlinear Characterization*. PhD thesis, West Virginia University, 2013.

- [13] Qinghua Huang and Zhaozheng Zeng. A review on real-time 3d ultrasound imaging technology. *BioMed Research International*, 2017:1–20, 2017.
- [14] Laurent Castera, Xavier Forns, and Alfredo Alberti. Non-invasive evaluation of liver fibrosis using transient elastography. *Journal of Hepatology*, 48(5):835–847, May 2008.
- [15] Ji Hoon Jang, Morten Fischer Rasmussen, Anshuman Bhuyan, Hyo-Seon Yoon, Azadeh Moini, Chienliu Chang, Ronald D Watkins, Jung Woo Choe, Amin Nikoozadeh, Douglas Stephens, Omer Oralkan, Kim Butts Pauly, and Butrus Khuri-Yakub. Dual-mode integrated circuit for imaging and HIFU with 2-d CMUT arrays. In *2015 IEEE International Ultrasonics Symposium (IUS)*. IEEE, October 2015.
- [16] Grand View Research. Medical imaging market size, share and trend analysis report by product (x-ray, computed tomography, ultrasound, mri, nuclear imaging), by end use, by region, and segment forecasts, 2021 - 2028, 2020.
- [17] Fraunhofer Institute for Photonic Microsystems. Mems report, 2013.
- [18] Muhammed Sabri Salim, M.F. Abd Malek, R.B.W. Heng, K.M. Juni, and Naseer Sabri. Capacitive micromachined ultrasonic transducers: Technology and application. *Journal of Medical Ultrasound*, 20(1):8–31, March 2012.
- [19] Laurent Sandrin, Bertrand Fourquet, Jean-Michel Hasquenoph, Sylvain Yon, Céline Fournier, Frédéric Mal, Christos Christidis, Marianne Ziol, Bruno Poulet, Farad Kazemi, Michel Beaugrand, and Robert Palau. Transient elastography: a new noninvasive method for assessment of hepatic fibrosis. *Ultrasound in Medicine & Biology*, 29(12):1705–1713, December 2003.
- [20] Claudia Randazzo, Anna Licata, and Piero Luigi. Liver biopsy - indications, procedures, results. In *Liver Biopsy - Indications, Procedures, Results*. InTech, November 2012.
- [21] Diagnosis of cirrhosis, Mar 2018.
- [22] Johns Hopkins Medicine. "Common Liver Tests".
- [23] Suk Keu Yeom. Prediction of liver cirrhosis, using diagnostic imaging tools. *World Journal of Hepatology*, 7(17):2069, 2015.
- [24] N. Frulio and H. Trillaud. Ultrasound elastography in liver. *Diagnostic and Interventional Imaging*, 94(5):515–534, May 2013.

- [25] Scott L. Friedman. Liver fibrosis – from bench to bedside. *Journal of Hepatology*, 38:38–53, January 2003.
- [26] T. J. Dubinsky, C. Cuevas, M. K. Dighe, O. Kolokythas, and J. H. Hwang. High-intensity focused ultrasound: current potential and oncologic applications. *AJR Am J Roentgenol*, 190(1):191–199, Jan 2008.
- [27] P. A. LINDSTROM. Prefrontal ultrasonic irradiation-a substitute for lobotomy. *AMA Arch Neurol Psychiatry*, 72(4):399–425, Oct 1954.
- [28] W. J. FRY, F. J. FRY, J. W. BARNARD, R. F. KRUMINS, and J. F. BRENNAN. Ultrasonic Lesions in the Mammalian Central Nervous System. *Science*, 122(3168):517–518, 1955.
- [29] Yu-Feng Zhou. High intensity focused ultrasound in clinical tumor ablation. *World Journal of Clinical Oncology*, 2(1):8, 2011.
- [30] Lauren Mancia, Eli Vlaisavljevich, Zhen Xu, and Eric Johnsen. Predicting Tissue Susceptibility to Mechanical Cavitation Damage in Therapeutic Ultrasound. *Ultrasound in Medicine & Biology*, 43(7):1421–1440, 2017.
- [31] Z. Izadifar, Z. Izadifar, D. Chapman, and P. Babyn. An Introduction to High Intensity Focused Ultrasound: Systematic Review on Principles, Devices, and Clinical Applications. *J Clin Med*, 9(2), Feb 2020.
- [32] B. B. Goldberg, R. Gramiak, and A. K. Freimanis. Early history of diagnostic ultrasound: the role of American radiologists. *AJR Am J Roentgenol*, 160(1):189–194, Jan 1993.
- [33] Aladin Carovac, Fahrudin Smajlovic, and Dzelaludin Junuzovic. Application of Ultrasound in Medicine. *Acta Informatica Medica*, 19(3):168, 2011.
- [34] B. Cox. "Acoustics for ultrasound imaging". in Lecture Notes, London:University College, 2012.
- [35] George D. Ludwig. The velocity of sound through tissues and the acoustic impedance of tissues. *The Journal of the Acoustical Society of America*, 22(6):862–866, November 1950.
- [36] Inge Edler and Kjell Lindström. The history of echocardiography. *Ultrasound in Medicine & Biology*, 30(12):1565–1644, December 2004.
- [37] Armen P. Sarvazyan, Matthew W. Urban, and James F. Greenleaf. Acoustic waves in medical imaging and diagnostics. *Ultrasound in Medicine & Biology*, 39(7):1133–1146, July 2013.

- [38] Peter Burgholzer, Johannes Bauer-Marschallinger, Bernhard Reitingner, and Thomas Berer. Resolution limits in photoacoustic imaging caused by acoustic attenuation. *Journal of Imaging*, 5(1):13, January 2019.
- [39] Arinc Ozturk, Joseph R. Grajo, Manish Dhyani, Brian W. Anthony, and Anthony E. Samir. Principles of ultrasound elastography. *Abdominal Radiology*, 43(4):773–785, February 2018.
- [40] Nimrod M Tole, Harald Ostensen, World Health Organization, et al. Basic physics of ultrasonic imaging/by nimrod m. tole; editor: Harald ostensen. In *Basic physics of ultrasonic imaging/by Nimrod M. Tole; Editor: Harald Ostensen*. 2005.
- [41] R. S. Goertz. Ultraschallelastographie. *Der Radiologe*, 55(11):949–955, October 2015.
- [42] G. ter Haar. *The safe use of ultrasound in medical diagnosis*. British Institute of Radiology, 2012.
- [43] Vibration-controlled transient elastography (vcte). White Paper, .
- [44] Wen Zhang, Hui Zhang, Shijiu Jin, and Zhoumo Zeng. A two-dimensional CMUT linear array for underwater applications: Directivity analysis and design optimization. *Journal of Sensors*, vol. 2016:8 pages, 2016.
- [45] Rui Zhang, Chenyang Xue, Changde He, Yongmei Zhang, Jinlong Song, and Wendong Zhang. Design and performance analysis of capacitive micromachined ultrasonic transducer (CMUT) array for underwater imaging. *Microsystem Technologies*, 22(12):2939–2947, November 2015.
- [46] Benedikt Kohout (2021). Transducer Array Calculation (TAC) GUI (<https://www.mathworks.com/matlabcentral/fileexchange/35657-transducer-array-calculation-tac-gui>), Matlab Central File Exchange, Retrieved February 28, 2021.
- [47] Timothy A. Bigelow, Charles C. Church, Kurt Sandstrom, John G. Abbott, Marvin C. Ziskin, Peter D. Edmonds, Bruce Herman, Kai E. Thomenius, and Tat Jin Teo. The thermal index. *Journal of Ultrasound in Medicine*, 30(5):714–734, May 2011.
- [48] Mosaddequr Rahman, Jonathan Hernandez, and Sazzadur Chowdhury. An improved analytical method to design CMUTs with square diaphragms. *IEEE Transactions on Ultrasonics, Ferroelectrics, and Frequency Control*, 60(4):834–845, April 2013.
- [49] R. Manwar, L. Arjunan, M. Ahmadi, and S. Chowdhury. Resonant frequency calculation of square diaphragms: A comparison. In *2015 IEEE 6th Latin American Symposium on Circuits Systems (LASCAS)*, pages 1–4, 2015.

- [50] Arif S. Ergun, Goksen G. Yaralioglu, and Butrus T. Khuri-Yakub. Capacitive micromachined ultrasonic transducers: Theory and technology. *Journal of Aerospace Engineering*, 16(2):76–84, April 2003.
- [51] Matthew Meloche. A mems non-planar constant beamwidth ultrasonic sensor microarray, 2007.
- [52] G. G. "Yaralioglu, A. S. Ergun, B. Bayram, E. Haeggström, and B. T. " Khuri-Yakub. Calculation and measurement of electromechanical coupling coefficient of capacitive micromachined ultrasonic transducers. *"IEEE Trans Ultrason Ferroelectr Freq Control"*, "50"("4"):"449–456", "Apr" "2003".
- [53] Ramón Bataller and David A. Brenner. Liver fibrosis. *Journal of Clinical Investigation*, 115(2):209–218, February 2005.
- [54] Karen Wallace, Alastair D. Burt, and Matthew C. Wright. Liver fibrosis. *Biochemical Journal*, 411(1):1–18, March 2008.
- [55] Zahra Izadifar, Zohreh Izadifar, Dean Chapman, and Paul Babyn. An introduction to high intensity focused ultrasound: Systematic review on principles, devices, and clinical applications. *Journal of Clinical Medicine*, 9(2):460, February 2020.
- [56] J.A. Jensen and N.B. Svendsen. Calculation of pressure fields from arbitrarily shaped, apodized, and excited ultrasound transducers. *IEEE Transactions on Ultrasonics, Ferroelectrics and Frequency Control*, 39(2):262–267, March 1992.
- [57] Hyo-Seon Yoon, Srikant Vaithilingam, Kwan Kyu Park, Amin Nikoozadeh, Kamyar Firouzi, Jung Woo Choe, Ronald D. Watkins, Huseyin Kagan Oguz, Mario Kupnik, Kim Butts Pauly, and Pierre Khuri-Yakub. A 1-MHz 2-d CMUT array for HIFU thermal ablation. Author(s), 2017.
- [58] Jørgen Arendt Jensen. Field: A program for simulating ultrasound systems. In *10TH NORDICBALTIC CONFERENCE ON BIOMEDICAL IMAGING, VOL. 4, SUPPLEMENT 1, PART 1*:351–353, pages 351–353, 1996.
- [59] Jørgen Arendt Jensen and Peter Munk. Computer phantoms for simulating ultrasound b-mode and CFM images. In *Acoustical Imaging*, pages 75–80. Springer US, 1997.
- [60] L. Sandrin, M. Tanter, J.-L. Gennisson, S. Catheline, and M. Fink. Shear elasticity probe for soft tissues with 1-d transient elastography. *IEEE Transactions on Ultrasonics, Ferroelectrics and Frequency Control*, 49(4):436–446, April 2002.

- [61] Rosa M.S. Sigrist, Joy Liao, Ahmed El Kaffas, Maria Cristina Chammas, and Juergen K. Willmann. Ultrasound elastography: Review of techniques and clinical applications. *Theranostics*, 7(5):1303–1329, 2017.

Vita Auctoris

NAME:	Sauparno Debnath
PLACE OF BIRTH:	West Bengal, India
YEAR OF BIRTH:	1993
EDUCATION:	Maulana Abul Kalam Azad University of Technology (formerly known as West Bengal University of Technology), West Bengal, India 2015, Bachelor of Technology Electrical Engineering University of Windsor Windsor, Ontario, Canada 2021, Master of Applied Science Electrical and Computer Engineering